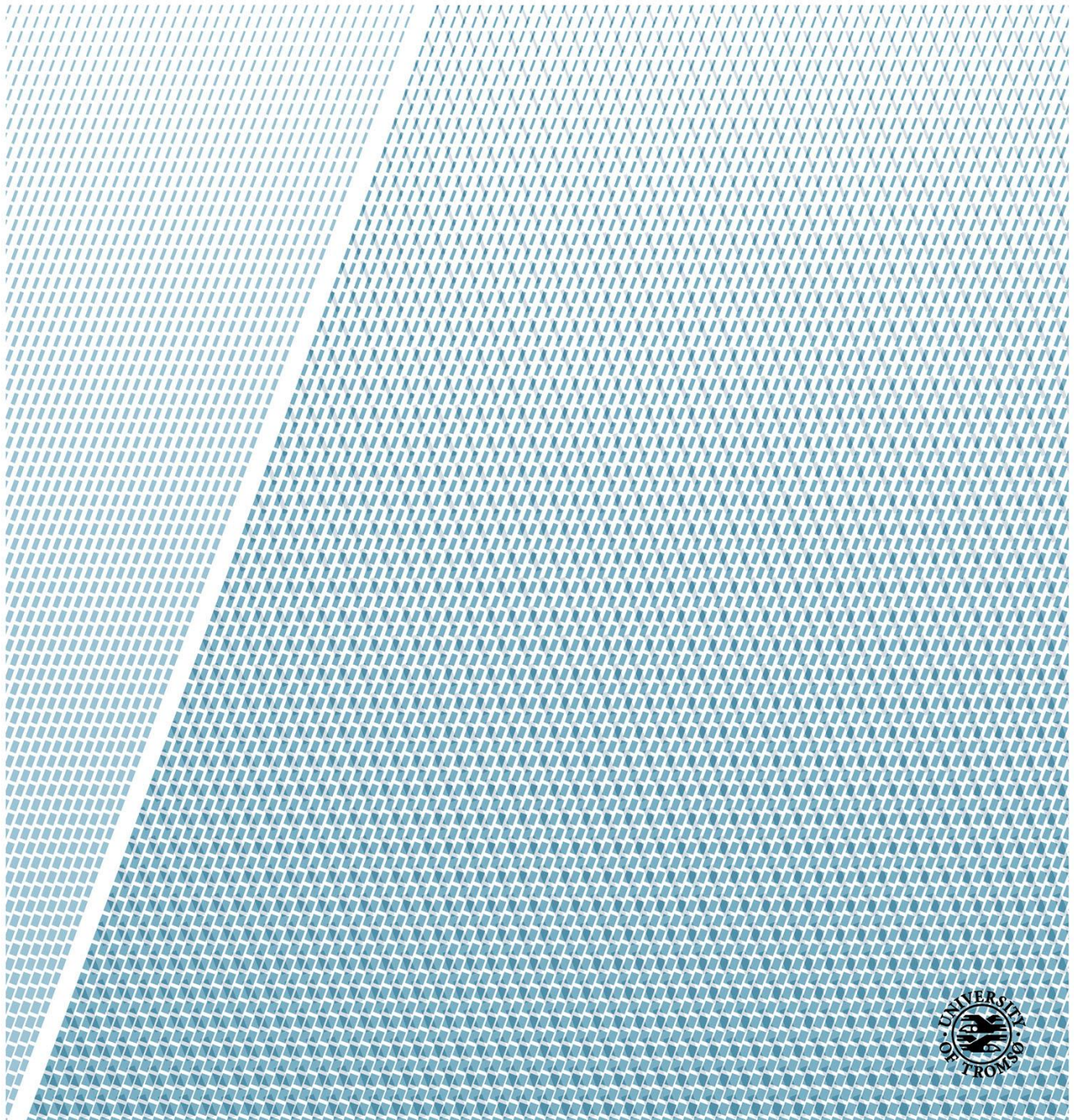# Ocean Modeling in Northern Norway: A Tidal Verification Study

—

Hans Kristian Djuve
EOM-3901 Master's Thesis in Energy, Climate and Environment

June 2014

Abstract

The coast of Northern Norway has for the first time been modeled using an unstructured grid. The modeling is done using two separate grids of different resolution, and the model data is compared to measurements done along the coast to verify its performance for both the fine and coarse grid. The model is a 2-D depth integrated model of tidal circulation with bottom friction. The data have been analyzed and the model replicates the amplitude of the main tidal constituent M_2 with an accuracy of about 95%, with the coarse grid surprisingly yielding slightly better results than the finer grid. The reason for this is believed to be because the southern boundary limit in the fine grid is located at an inconvenient area.

For the tidal currents modeled, the accuracy has been shown to be significantly lower. The magnitude of the velocity is in many cases correctly modeled, but with larger errors in the direction. M_2 and N_2 are generally modeled at slightly too high velocities while S_2 and K_1 are generally modeled at slightly too low velocities. The model impresses in the way that it in general perform just as good within a fjord or at other complex geometries, as it does close to the open sea. The model also perform equally good both at locations with strong and weak currents.

Acknowledgments

This thesis has been an interesting dive into the field of ocean modeling and physical oceanography, and I am really grateful for all I have learned. First of all I would like to thank my supervisor Ole Anders Nøst for continuously providing me with ideas and for ways to tackle challenges that have appeared underways, and for providing me with invaluable knowledge within the field. I would also like to thank Øyvind and Frank at Akvaplan for their help with Matlab and with sorting out data, and Yngve Birkelund for contributing in formulating the project task.

I also owe my thanks to the rest of the students at Norut-brakka for enjoyable breaks within all the hard work a thesis is, including food, laughter, cookies and games^{lol}. A special thanks to Mike for sharing his vast Matlab and LaTeX knowledge when not even google is of any help.

Last I would like to thank my beautiful Christel for being there for me and making sure I have a life outside my office, and our awesome son Ciljan for always greeting me with a big smile when I come home after a long day at the office. The two of you makes my life truly enjoyable.

Contents

List of Figures

List of Tables

Chapter 1

Introduction

The effect of the tide reaches all across the globe, and is of great importance for people dependent on the ocean. Fish moves according to tide, certain areas can only be passed by boat when there is high-tide, and in areas with narrow passages and a significant tidal amplitude, green dependable energy can be harvested. Humans have tried to understand the driving forces causing the tidal variations for thousand of years, yet it was not until the 17th century the proper physical description of the tides was formulated [Pugh, 1987]. Since then, numerous advances has been made in the field, and in the last decades the focus has mostly been towards numerical modeling aspect of the tide, which also is the focus of this thesis. The main driving force behind this is the fact that computational power has increased drastically the last decades. This, together with the fact that new and more efficient methods within computational fluid dynamics (CFD) are continuously being developed, allows for higher resolution and more efficient computation when modeling [Tu et al., 2013].

Akvaplan-niva, a firm working with aquaculture and ocean environment is supporting this thesis with measurement data, model data and guidance. To have a realistic model is core to much of the work done at Akvaplan-niva, where they are using ocean models to detect areas with high rate of water-flow bringing nutritious and oxygen rich water into the fjords, and to avoid waste to build up below the fish farm. How the spread of infection between fish farms takes place might also be better understood and traced using a model. It is also of interest to see how waste and pollution from cities along the coast is distributed in the local coastal area due to the tidal streams present.

The model used until now at Akvaplan-niva is the 3-D Regional Ocean Modeling System (ROMS) [Shchepetkin and McWilliams, 2005], which uses a structured grid. Structured grids can be problematic when modeling coastal areas with complex geometry. When doubling the resolution of a structured grid, the computational time increases approximately eight times, and locally increasing the resolution while maintaining good numerical properties is challenging [Debreu and Blayo, 2008]. However, there are models using unstructured grids which might yield better results. One such model is the Finite-Volume Community Ocean Model (FVCOM) [Chen et al., 2003], and this model is applied to the coast of Northern Norway and the goal of this thesis is to test and verify the model. The focus will be on how the model manages to reproduce the tidal effects observed along the coast, both with respect to elevation and tidal currents. Two grids will be compared, one coarse and one fine to determine the importance of high resolution to obtain proper results.

1

1.1 Related work

Tidal model verification can, and has been done using a variety of different methods. No one has ever used an unstructured grid for modeling the tide along the North Norwegian coast before. The Norwegian coast has a multitude of fjords and islands, and the complex geometry is hard to model properly using a structured grid.

1.1.1 Previous FVCOM applications

The ocean model FVCOM has been validated and tested versus several different other ocean models using a structured grid. When applied to the Bohai Sea at the northern coast of China, FVCOM provided a better simulation than a structured model named "Estuarine, Coastal and Ocean Model (semi-implicit)" or ECOM-si which was applied to the same domain with same initial conditions [Chen et al., 2003]. The Bohai Sea is rather shallow with mean depth of 20 meters, and there are several islands there which increase the need of a good geometric fitting for a more accurate simulation of the tide, and this is believed to be the reason FVCOM provided better results [Chen et al., 2003].
In ECOM-si, a uniform horizontal resolution of 2 km was used in most of the model domain but not near the open boundary where the resolution was set to 7 km. In FVCOM the resolution was set to 2.6km around the coast, and around 17 km close to the open boundary [Chen et al., 2003].

FVCOM has also been tested towards the much used Regional Ocean Modeling System (ROMS), and for simple idealized domains, the accuracy of the two models is similar [Huang et al., 2008]. In a highly nonlinear case, the second order solution scheme used in FVCOM provides almost as good accuracy as the fourth-order scheme used in ROMS, given the horizontal resolution is high. However, the FVCOM solution is less computational heavy, and new numerical techniques within the field of computational fluid dynamics can be used in FVCOM to further improve its performance.

A version of FVCOM focusing on the Arctic Ocean (AO-FVCOM) has also been developed, and the Norwegian coast is included in this model. The horizontal resolution used here is 1km in near-coast areas to 15km in the deep ocean. The model is run with the diurnal constituents K_1 and O_1, and the semidiurnal constituents S_2 and M_2 [Chen et al., 2009]. Results from the simulation using this model did agree well with available observational data with regard to the magnitude of the four mentioned constituents. However, the results suggest that to reproduce realistic tides in the Arctic Ocean phase-wise (especially in winter time), accurate simulation of water stratification and ice is crucial. This is an obstacle as it is challenging for a model to take into account internal tides and complex ice dynamics [Chen et al., 2009].

1.1.2 Ocean models in Norway

Lofoten model

The larger of the two grids used in this thesis includes the Lofoten islands, and this area has been modeled before by Moe, Ommundsen and Gjevik [Moe et al., 2002]. They used a depth integrated model with 500 meter horizontal resolution and included the constituents M_2, S_2, N_2 and K_1. The boundary conditions in this model comes from interpolation from a large-scale tidal model covering the Nordic Seas, and are implemented with the flow relaxation scheme explained in [Engedahl,

1995]. The best fit in this model was found to be for the M_2 component, with a standard deviation between observed and modeled amplitude and phase of 2.3 cm and 2.5° [Moe et al., 2002]. There are several reasons for why the area around Lofoten is, and has been of interest for a long period of time. The Maelstrom vortex know as Moskenstraumen has been known for centuries for its mythical capacity to swallow ships, and has been mentioned by world famous writers such as Jules Verne and Edgar Allan Poe [B, 2001]. In the later years it was realized that such oceanographic elements as tidal streams had an major effect on cod spawning and development of eggs and larvae in the area around Lofoten [Eggvin, 1932] [Eggvin, 1934]. The newest interest in the strong currents in the area around Lofoten is with regard to tidal power.

The tidal amplitude along the coast of Norway is increasing northwards, until it reaches Lofoten, where the amplitude of the tidal wave drops before its start building up again as it travels further north-east towards Russia, as seen on Figure 1.1 The reason for the tidal wave amplitude drop is
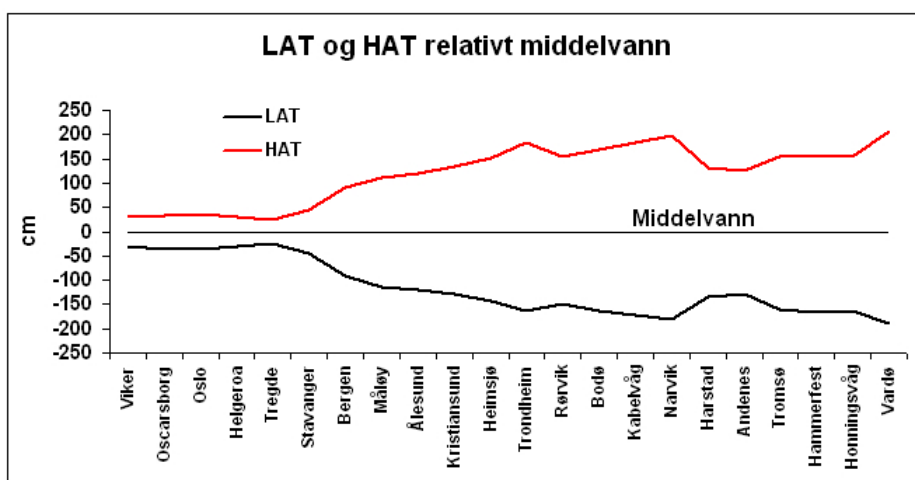
Figure 1.1: LAT= Lowest astronomical tide, HAT=Highest astronomical tide. Taken from http://vannstand.no/images/articles/ fakta/image14.gif, taken 15.12.2013

believed to be a combination of (1) the narrowing of the continental shelf west of Lofoten, (2) a tidal choking phenomenon caused by the group of islands providing a blocking effect and (3) the split up of the tidal shelf wave, where one part heads north along the continental slope towards Svalbard, while the other continue along the coast eastwards, towards Vardø [Grabbe et al., 2009].

The Bergen Ocean Model(BOM)

BOM was used by [Eliassen et al., 2001] to study the circulation in three locations located just south of Lofoten, not far from the city Bodø. BOM uses a structured grid, and is a σ-coordinate 3-D model. The main advantage of such a model is the ability to resolve bottom boundary and surface layers, but might struggle with exhibiting correct internal pressure gradients under circumstances such as steep bottom topography [Berntsen, 2002] [Grabbe et al., 2009]. The model also makes use of the hydrostatic and Boussinesq approximations. The two assumptions are not relevant when doing 2-D depth integrating modeling, but with 3-D modeling, they might play a significant role, even though the hydrostatic and Boussinesq approximations are often used. The hydrostatic

approximation is the assumption that the pressure at a given point is only due to the weight of the water above the point [Azerad and Guillen, 2001], while the Boussinesq approximation is that the density variation is not big enough to affect inertia but may be important with regard to buoyancy effects [Gray and Giorgini, 1976] .

1.1.3 Structure of the thesis

This thesis consists of six chapters. In Chapter 2: Ocean tides and the forces causing it, the basic theory behind ocean tides is explained with the relationship between the gravitational pull and centrifugal force. How the contribution from the Moon and Sun is calculated is also briefly discussed and the eight major tidal constituents are represented

In Chapter 3, the principles behind tidal signal decomposition and constituent extraction is explained. The chapter also include a brief description of the matlab package Utide used for tidal analysis in this study, alongside an explanation of the process from obtaining the data to produce results that can be discussed.

The next chapter introduces the equations describing water flow, and their FVCOM adapted versions which arises from depth integration and certain assumption in the 2-D case. The grid properties and bottom friction is also explained.

The following Chapter 5 includes the results from the tidal analysis and model simulations for the different locations studied and for the two different grids used. Both analysis of pressure data and velocity data is represented accompanied with a brief discussion of the results

Last, in Chapter 6 the conclusion together with suggestions to further work within the field can be found.

Chapter 2

Ocean tides and the forces causing it

The rise and fall of sea level, often refereed to as tide, is propagating around the Earth as a shallow water wave with a wavelength much larger than the depth of even the deepest ocean. Wave height H is the vertical change in height between the crest and trough, while the amplitude is $A = H/2$ and frequency f is the number of wave peaks passing a fixed point in space per second. Wavelength λ is given as the distance between one wave crest or through, to the next one, and this ranges from meters for wind waves to hundreds of kilometers for tide waves. Waves are divided into two main types: shallow water waves and deep water waves. A wave is considered a deep water wave if water depth $d \geq \lambda/2$ [Colling et al., 1989]. The water particles in this type of waves moves in a almost circular motion with a diameter that decreases with depth, and it drifts forward ever so slightly with what is called Stokes drift, which also decreases with depth. This is not to be confused with the movement of the actual waveform, which propagates at a much higher rate. The other type of waves are the shallow water waves, and waves fall under this category when $d < \lambda/20$ [Colling et al., 1989].Tidal waves are shallow water waves and thus travels at the speed v=$\sqrt{gd}$, where g is the gravitational constant. The motion of particles in this type of waves are more elliptic, as they are compressed in the vertical direction by the presence of the ocean floor, and as the depth increases, the vertical diameter goes towards 0, resulting in a back and forward motion near the bottom. See Figure 2.1 for illustrations. It is worth mentioning that Kelvin waves are an important wave-type when considering the tide, as the tidal wave propagates similar to Kelvin waves. Kelvin waves are the waves in the ocean that balances the Earth's Coriolis force against coastlines or other topographic boundaries [Pugh, 1987].
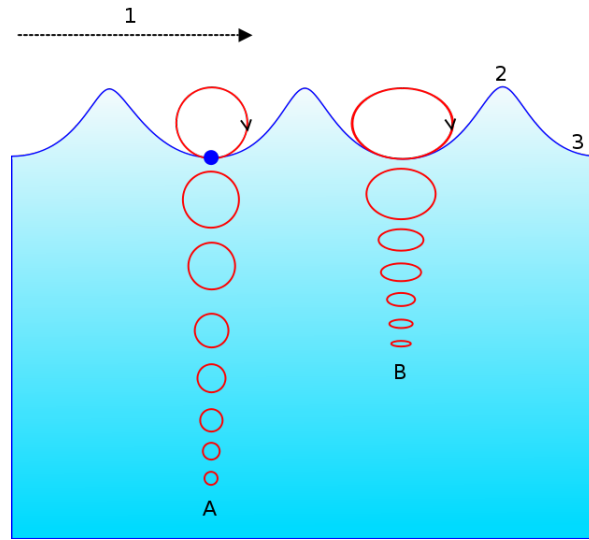
Figure 2.1: Wave particle motion in deep (A) and shallow (B) water, from http://en.wikipedia.org/wiki/Wave_power taken 19.10.2013

2.1 Tide theory

Tide is the periodic rise and fall of sea-level, mainly caused by gravitational pull from the moon and the sun. The main contribution comes from the Moon, which together with the Earth forms a system rotation around a common center of mass(located within the Earth), with a period of 27.3 days. Planet Earth will revolve eccentrically with respect to the center of mass of the Earth-Moon system. This means all points on and within the Earth will have the same angular velocity $(2\pi/27.3days)$ and will experience the same acceleration, thus equal centrifugal force which will be parallel to a line drawn between the center of the Earth and the center of the Moon. The magnitude of the gravitational pull on the Earth from the Moon is given by the following equation (2.1)

$$F_G = G\frac{m_1 m_2}{R^2} \tag{2.1}$$

where G is the universal gravitational constant and R is the distance between the two bodies with mass m_1 and m_2 [Colling et al., 1989]. Note the squared dependency on the distance between the two bodies, in this case the Earth and Moon, which is strongly dependent on where on the Earth this force is measured. The closer a point is to the Moon, the stronger the gravitational force exceeded on that point from the moon will be, and it will be in the direction of the center of the Moon. The difference between gravitation and acceleration results in the tide-generating forces illustrated in Figure 2.2 (note the arrows are not to scale). Figure 2.2 also illustrates why there is a high tide at the opposite side of the Earth to where the moon is. As the gravitational force due to the Moon is less on the side of the Earth facing away from the Moon, this force only cancels out a little part of the centrifugal force, hence a high tide forms both where the Earth is directly facing and facing away from the Moon. In theory this should result in two high tides per day(or more precisely each 24h and 50min which is the duration of a lunar day) wherever there
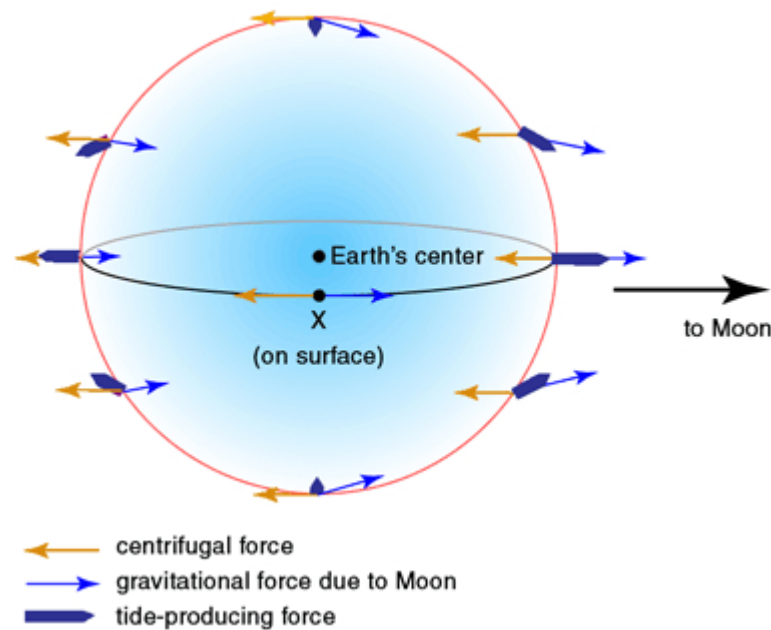
Figure 2.2: From http://www.oc.nps.edu/nom/day1/partc.html, taken 09.11.2013

is an ocean, and the two tides should be at approximately the same size. This phenomenon is called semi-diurnal lunar tides, and is denoted by the constituent M_2. However, because of all the land masses and shallow water areas on the planet denying the tidal wave to keep up with the gravitational forces, this is not the case for most part of the planet. The most common is to have two uneven high and low tides each day, called mixed semi-diurnal tides. There are also places where there is just one high and one low tide each day, and phenomenon is called diurnal tide.

The other contributer is the Sun, and even though its force on Earth is close to 175 times stronger than that from the Moon (from using equation 2.1), only a fraction of this force comes into play when considering the effect it has on the tide. Because it is so far away, the variation in the tidal forces from the point on Earth closest to the Sun and the point furthest from the Sun is rather small, and again by using equation 2.1 it can be found that the force from the sun which influence the tide is only about 0.43 times that of the Moon. This gives rise to a second semi-diurnal tidal constituent named S_2. From the same reason the Moon creates two tides, so does the Sun, and when the Moon, the Sun and the Earth is aligned the result is called spring tide, and this is when the biggest tide-waves occur. On the other hand, imagine a line drawn from the Moon center to Earth center, and another one from the Sun center to the Earth center. When the lines are perpendicular the smallest tide-waves occur, and this is called neap tide. This is illustrated in Figure 2.4 (note that the water columns illustrated are not to scale). In Figure 2.3 pressure data from a 31 day long time series can be seen, and the gravitational pull caused when the moon and sun are in line is clearly visible in the sample.

7
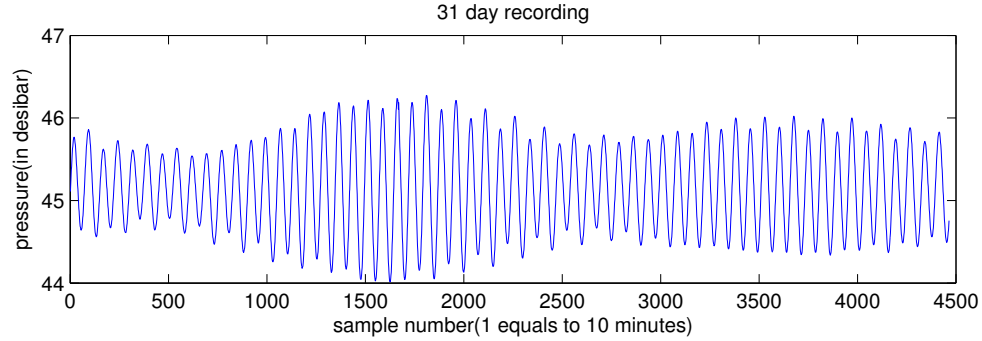
Figure 2.3: Record sample.

Tidal Species	Name	Period(hr)
Semidiurnal		
Principal lunar	M_2	12.4206
Principal solar	S_2	12.0000
Lunar elliptic	N_2	12.6584
Lunisolar	K_2	11.9673
Diurnal		
Lunisolar	K_1	23.9344
Principal lunar	O_1	25.8194
Principal solar	P_1	24.0659
Elliptic lunar	Q_1	26.8684

Table 2.1: The eight major tidal constituents

Tidal constituents

The eight tidal constituents listed below in Table 2.1 are the most dominant ones, and they are also the only constituents included in the model FVCOM discussed in detail in Chapter 4. The period is related to the orbital frequency of the Moon and the Sun relative to the Earth.

Tide dynamics

Ideally, there is high tide directly below the moon at all times. This would have been the case if on Earth, the tide experienced was the equilibrium tide. However, because of the varying ocean depth, land masses, rate of Earth rotation and the Coriolis force, tide at most latitudes lag behind the passage of the Moon [Colling et al., 1989]. This increases the complexity of creating exact numerical models of the tide.

The effect of the tide on lakes is minimal. This is because the difference in gravitational pull from one end of the lake to the other is negligible, and for the biggest lakes will give an effect of only a few centimeters. The reason a more or less "global" ocean is needed, is that the difference in gravitational pull is only large enough when considering the difference between the force on the side facing the Moon, and the side facing away. Because of this, when modeling a limited area, say the

coast of Northern Norway, the boundary conditions are critical. If they are not considered, the tide will only vary on the scale of cm, as if it was a lake which would result in major errors. To solve this issue, the normal procedure is to import boundary conditions from a global ocean model, then make a fine grid for the area of interest to increase the detail level to obtain a model which is as close to reality as possible. In theory, it could be possible to model the global ocean with a fine grid. In reality however, this would require immense computational power and time, which is the reason why it is not a realistic option. Also the process of generating a fine grid along a complex coastline with islands and fjords is a time consuming task.

Figure 2.6 Diagrammatic representation of the interaction of the solar and lunar tides, as seen from above the Earth's North Pole.
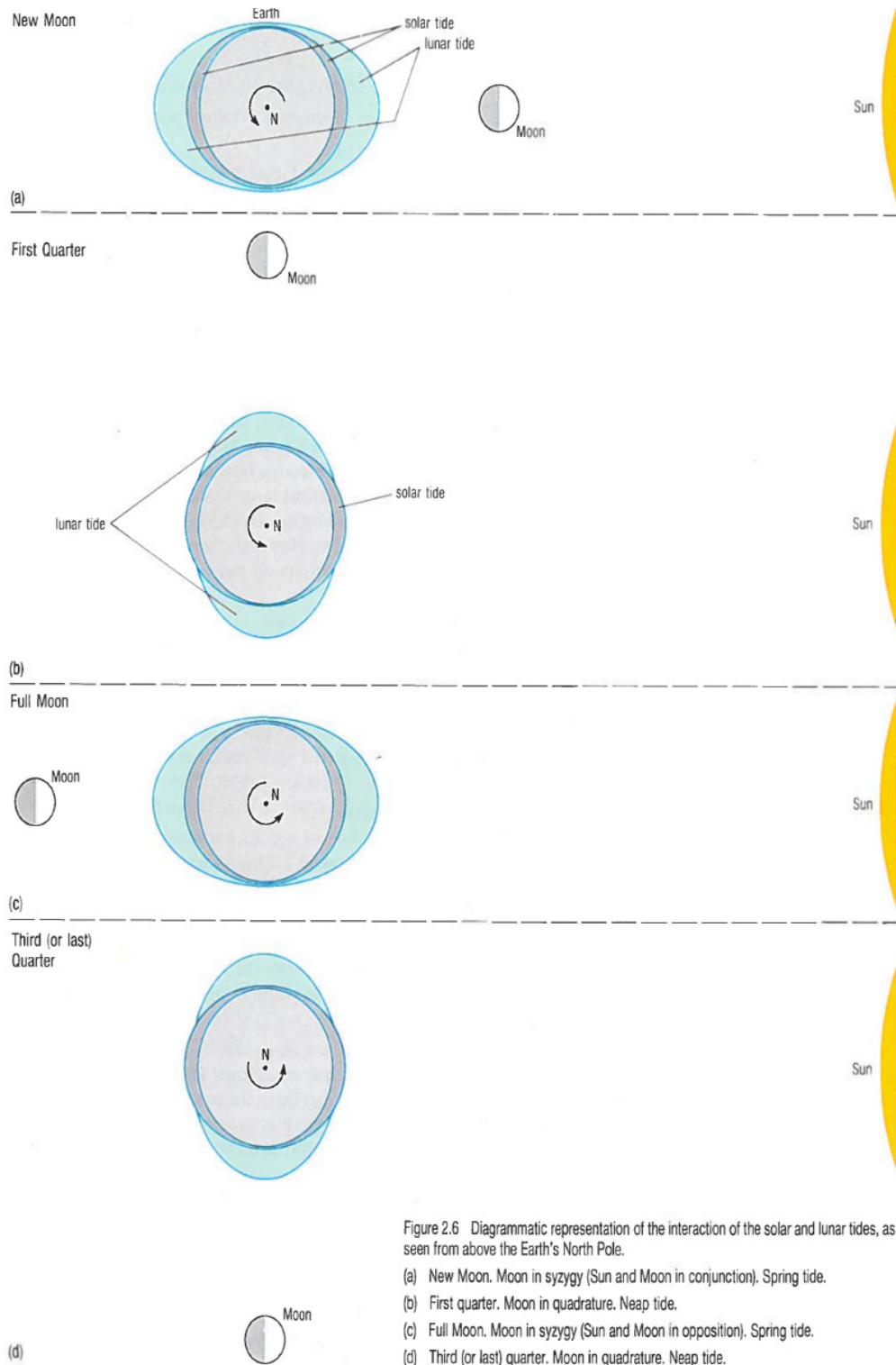
(a) New Moon. Moon in syzygy (Sun and Moon in conjunction). Spring tide.
(b) First quarter. Moon in quadrature. Neap tide.
(c) Full Moon. Moon in syzygy (Sun and Moon in opposition). Spring tide.
(d) Third (or last) quarter. Moon in quadrature. Neap tide.

Figure 2.4: From [Colling et al., 1989]

Chapter 3

Data analysis

In this chapter, the process of analyzing data will be introduced. Both model data and measurement data is analyzed in Matlab. The goal is to extract the different tidal constituents which contributes the most to the observed tide, and use this to analyze how well the model replicates the tidal effects along the coast of Northern Norway.

The instrument mostly used to collect tidal data from sites is called Seaguard, and is using Doppler to measure the velocity, with an accuracy of $\pm$ 1%, and with a resolution of 0,1mm/s. It is capable of reading velocities in the range of 0 - 3m/s. Measured values are stored every 10 minutes, and the value stored is averaged over 2.5 minutes. Some of the Seaguard instruments are also equipped with pressure sensors.
The other instrument is a rotor instrument, which is propel based. The accuracy is $\pm$1cm/s and it works in the range from 2 to 295 cm/s, so at low current velocities, this instrument is not ideally to use.

3.1 Extraction of tidal constituents

The tidal wave can be considered a wave formed by many smaller amplitudes and phases, and depending on how the phases are synchronized with each other, the tidal amplitude varies. In the case of synchronized phases, high tide will be the result, while the opposite will be the case when the phases are out of sync. When considering the water height (or pressure), varying in time because of the tide, it can be compactly represented using superposition of the constituents in the following way:

$$h(t) = \sum A_i sin \left(\frac{2\pi t}{T_i} + g_i \right) \qquad (3.1)$$

where A_i,g_i and T_i are the amplitude, phase and period of tidal constituent i [Polagye, 2013]. Note that this is only if the data is centered with mean equal to zero.

Tides and tidal currents are unique in the way that the frequencies are known a priori, as they are determined by the very predictable movements of astronomical contributers(mainly the Sun, the Moon and the rotation of the Earth). The weather and the climate system however is in contrast rather chaotic and the repeated cycles(seasons, day and night etc) only play a smaller

part. So whereas tides are a periodic process, the weather and the processes behind it are stochastic processes involving random and non-periodic fluctuations [Parker, 2007]. When considering tidal data, time series analysis is central in processing the data, and the data can either be processed in time domain or frequency domain. Looking at the data in frequency domain, the most energy-rich frequencies will stand out, which for the majority of the Norwegian coast is M_2 and S_2. So the energy will be represented by a series of spikes at certain frequencies, and those frequencies are the tidal constituents. If noise from wind and atmospheric pressure is present in the data, this will appear as a smooth curve covering a broad range of frequencies, and thus will be easy to detect and avoid [Parker, 2007]. The downside with this approach is that no phase information can be found using spectral analysis, only the strength of the signal and importance of the diurnal and semidiurnal bands (which constituents that contribute the most). Hence the spectral results are of no use when tidal prediction is of interest. There are better ways of proceeding when analyzing tidal data, as all the frequencies are known beforehand(because of their astronomical origin), and this method will be described below.

For M_2 we know that the period is 12.4206 hours. Given a tidal data time series, it is rather simple to split it into 12.4206 hour long pieces, superimpose them and then average them. As the period of M_2 is unique, M_2 will be the only constituent in sync so the maximum will be at the same time within each 12.4206 hour long piece. If the time series is long enough, all other constituents will cancel themselves out. To Figure the required length of the time series to do so, it is necessary to calculate how long time it takes for the other constituents to go through a cycle in the divided tide data pieces. The following example illustrates this. S_2 has a period of 12.0000 hours, so the difference between M_2 and S_2 is 0.4206 hours. The amount of M_2 cycles needed for S_2 to cancel itself out is then $12/0.4206=28.5307$ M_2 cycles which in days is $28.5307*12.4206/24 = 14.77$. This leads to the well known Rayleigh's criterion, which indicates that the difference between two frequencies to resolve them must be greater than the inverse length of the data time series analyzed:

$$|\sigma_2 - \sigma_1| > T^{-1} \tag{3.2}$$

This has later been modified and the more updated version is the Munk and Hasselman criterion

$$|\sigma_2 - \sigma_1| > \frac{T^{-1}}{(signal/noise\ level)^{\frac{1}{2}}} \tag{3.3}$$

This method described above slightly resembles the Fourier-based harmoic analysis method which is actually used in programs to extract tidal constituents. Each tidal constituent is solved separately, and this was the first method used for harmoic analysis.

The least square technique

In modern harmonic analysis programs, the least square technique is the method most frequently used. This is a sort of optimization technique, which aims to minimizing the square difference between the original data series and the predicted series created using the calculated amplitude and phase lags which is estimated. There are many advantages with this method over the less used Fourier series method. There is no restriction to continuous equally spaced data with no gaps, it is more flexible when it comes to the length of the time series and to see the effect of adding more constituents to the analysis, and to see how the variance between the data time series and the predicted time series change in doing so [Parker, 2007].

Common regression techniques like least squares are based on maximum likelihood estimates, and

are often termed M-estimators [Fox, 2002]. Consider the linear model $h = Ax$, where h is the observed values, A is the basis function and x the set of unknown coefficients. In tidal analysis the system is overdetermined as the number of observations exceeds the number of constituents [Munk and Cartwright, 1966]. The goal is to seek a solution for x that minimizes an objective function ρ of the residual r, where $r = h - x^T A$. Typically, M-estimators minimizes

$$\sum_{i=1}^{n} \rho(r_i) = \sum_{i=1}^{n} \rho(h_i - x_i^T A). \tag{3.4}$$

taking the derivative of eq (3.4) and setting it equal to zero gives

$$\sum_{i=1}^{n} \psi(h_i - x_i^T A)x_i^T = 0 \tag{3.5}$$

where $\psi = \frac{\partial \rho}{\partial x}$. Defining the weight function ω as $\omega(r) = \frac{\psi(r)}{r}$ allows the estimating function to be written as

$$\sum_{i=1}^{n} \omega_i(h_i - x_i^T A)x_i^T = 0 \tag{3.6}$$

which will minimize the sum of weighted residuals

$$\sum_{i=1}^{n} \omega_i^2 r_i^2. \tag{3.7}$$

Equation (3.6) can then be solved as

$$x = (A^T \omega A)^{-1} A^T \omega h \tag{3.8}$$

or as

$$x = (A^T A)^{-1} A^T h \tag{3.9}$$

given ω is set to the diagonal of the identity matrix I. $A^T A$ is known as the sample correlation matrix [Theodoridis and Koutroumbas, 2008], and for ordinary least squares (OLS) equation (3.9) can be solved directly.

3.1.1 Utide

In this thesis, the matlab package Utide [Codiga, 2011] is used for tidal analysis and prediction. Utide has several options when it comes to which method to utilize when performing tidal analysis. The default one is a modified version of the least square method briefly described above, namely the robust iteratively-reweighted least squares(IRLS) soulution method investigated by [Leffler and Jay, 2009] which proved to reduce the confidence intervals compared to the ordinary least squares(OLS) method. The IRLS solution is obtained by iterative application of equation (3.8) using a weight function. See [Leffler and Jay, 2009] for the full text on IRLS.

Confidence interval

To determine the uncertainty factor when performing tidal analysis, confidence intervals are frequently used. Common for all the methods mentioned in this chapter is that they are all based on the assumption that all residual energy is noise. In short, a confidence interval is a interval estimate and is used to indicate how reliable an estimate is. Earlier a method explained by [Foreman, 1977] [Foreman and Henry, 1989] and [Godin, 1973] was used to compute the uncertainties of the cosine/sine model parameters, but it did not take into consideration the spectral nature of the residual hence it was more of a "white noise floor approach" [Codiga, 2011]. With white noise, it is assumed that the noise values have zero mean, the same Gaussian probability distribution and that they are mutually uncorrelated. Later a new method was developed by [Pawlowicz et al., 2002], and this was based on using spectral properties from the actual residual. Methods for determining the confidence intervals for the current ellipse parameters where also presented by [Pawlowicz et al., 2002]. Utide uses a generalized version of the methods introduced by Pawlowicz. Typical in this thesis the 95% confidence interval for the amplitude of the tidal constituents where found to be $\pm 1 * 10^{-4}$ to $1 * 10^{-7}$ meters.

Data acquisition

The model FVCOM is quite complex, and takes more than the average laptop to run. Stallo, the supercomputer at the University of Tromsø is used to run the model. The tidal constituents of interest must be defined, and which grid to use, before the model can be started. The model is in this study set to model 100 days, where the boundary inputs(amplitude and phase of the tidal constituent(s)) are gradually introduced over the first 10 days. The data extracted from the model is the last 34 days. To know the datalocations from the model to extract, the measurement data must be processed. This involves reading text and exel files of data into Matlab, and locating the coordinate of each location. Then the geographic coordinates gets converted to the coordinate system the model uses(UTM 33W). This is done to locate the nearest centroid in the case of velocity-data or nearest node in the case of elevation data that correspond to the actual location the measurement data has been obtained from. Now all the data is ready to be analyzed, which is done using Utide described in Chapter 3. During the post processing step, the tidal constituents of interest are extracted from both the model-data and measurement-data and the parameters describing them compared. This is constituent amplitude and phase in the case of pressure-data analysis, and u(east) and v(north) velocities and the elliptic parameters minoraxis, majoraxis and ellipse orientation angle θ. This process is illustrated in Figure 3.1

```
┌─────────────────────────┐
│   FVCOM simulation with  │
│ specified constituent(s) and │
│           grid           │
└─────────────────────────┘
             ↓
┌─────────────────────────┐   ┌─────────────────────────┐
│  Extracting parameters of │   │  Preprocess measurement  │
│         interest         │   │           data           │
└─────────────────────────┘   └─────────────────────────┘

             ↓                             ↓

┌───────────────────────────────────────────────────────┐
│                                                         │
│                    Post processing                      │
│              ┌─────────────────────────┐                │
│              │    Extracting tidal     │                │
│              │  constituents and their │                │
│              │       properties        │                │
│              └─────────────────────────┘                │
│                           ↓                             │
│              ┌─────────────────────────┐                │
│              │  Comparing results for  │                │
│              │  the different locations │                │
│              └─────────────────────────┘                │
│                                                         │
└───────────────────────────────────────────────────────┘
                           ↓
              ┌─────────────────────────┐
              │     Evaluate results     │
              └─────────────────────────┘
```
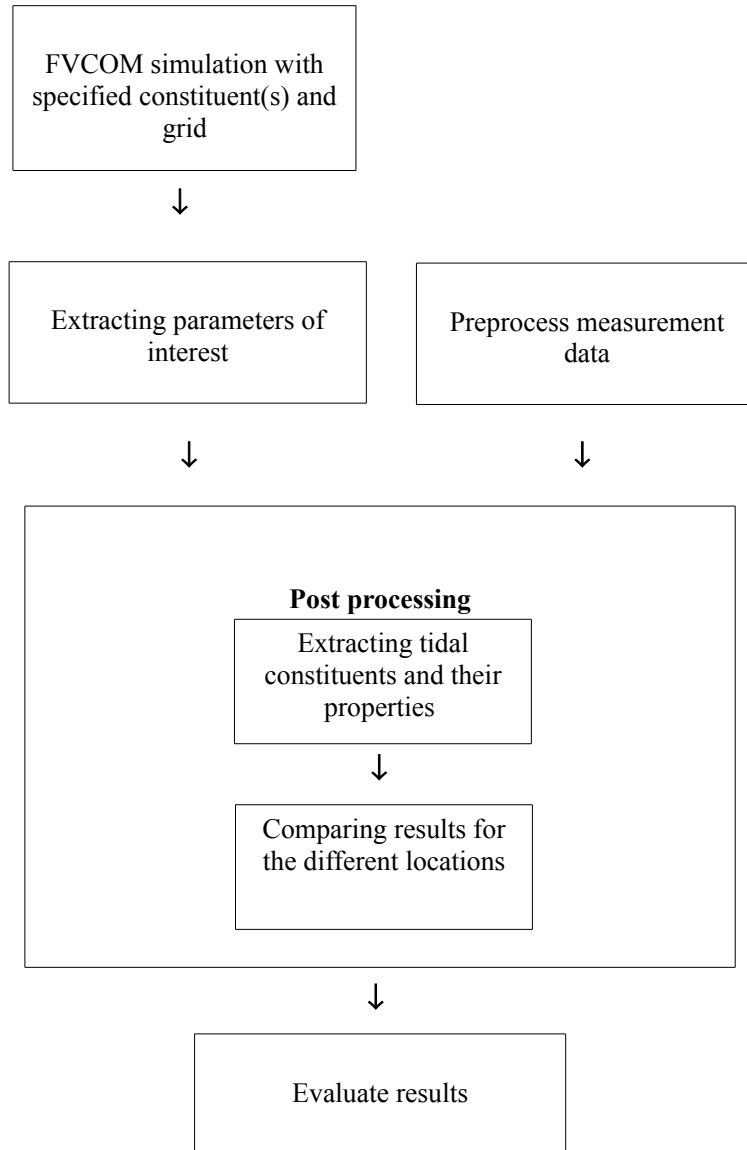
Figure 3.1: The process of data acquisition and data analysis summarized

15

Chapter 4

The theoretical foundation of FVCOM and grid properties

In this chapter, the most central equations behind the displacement of water caused by the tides, together with the governing equations behind FVCOM for ocean modeling will be explained for overview on the basics behind the model.

4.1 Continuity equation

One way to represent conservation of mass is with the following equation (4.1)

$$\frac{\partial \rho}{\partial t} + \frac{\partial (\rho u)}{\partial x} + \frac{\partial (\rho v)}{\partial y} + \frac{\partial (\rho w)}{\partial z} = 0 \tag{4.1}$$

where t is time, u,v, and w are current speed in the dimensions represented by x,y and z, while ρ is the water density [Parker, 2007]. However as ρ only varies from 1000kg/m^3 for freshwater and 1030kg/m^3 for salt water, a common simplification is to set $\rho = constant$ assuming an incompressible flow, and for 2-D modeling the density is not included as we integrate over the entire depth, so equation (4.1) is reduced to

$$\frac{\partial u}{\partial x} + \frac{\partial v}{\partial y} + \frac{\partial w}{\partial z} = 0 \tag{4.2}$$

which can be written on the compact form

$$\nabla \cdot \mathbf{V} = 0 \tag{4.3}$$

where

$$\mathbf{V} = u\mathbf{i} + v\mathbf{j} + w\mathbf{k}. \tag{4.4}$$

The governing momentum equations for x, y and z directions describing the flow in a tidal current can be written

$$\frac{Du}{Dt} + \frac{1}{\rho}\frac{\partial p}{\partial x} - fv = F_x \tag{4.5}$$

17

$$\frac{Dv}{Dt} + \frac{1}{\rho}\frac{\partial p}{\partial y} + fu = F_y \tag{4.6}$$

$$\frac{1}{\rho}\frac{\partial p}{\partial z} + g = 0 \tag{4.7}$$

where g is gravitational constant and f the Coriolis parameter

4.2 FVCOM governing equations

When adapting for 2-D modeling in FVCOM, the momentum equations from section 4.1 becomes

$$\frac{\partial u}{\partial t} + u\frac{\partial u}{\partial x} + v\frac{\partial u}{\partial y} + w\frac{\partial u}{\partial z} - fv = -\frac{1}{\rho_o}\frac{\partial P}{\partial x} + \frac{1}{\rho}\frac{\partial \tau_x}{\partial z} + F_u \tag{4.8}$$

for the u component of the momentum and

$$\frac{\partial v}{\partial t} + u\frac{\partial v}{\partial x} + v\frac{\partial v}{\partial y} + w\frac{\partial v}{\partial z} - fu = -\frac{1}{\rho_o}\frac{\partial P}{\partial y} + \frac{1}{\rho}\frac{\partial \tau_y}{\partial z} + F_v \tag{4.9}$$

for the v component. Here F_u and F_v represents horizontal momentum diffusion terms [Chen et al., 2003], while τ_x and τ_y represents the stress formed by vertical shear of the velocities. The momentum and continuity equations are then vertically integrated to be able to use for 2-D model setup. When depth integrating, the velocities becomes mean velocity, from top to bottom in the water column, and the aspect of stratification is neglected. Also, τ_x and τ_y becomes horizontal friction in u and v direction.

The depth integrated equations in a Cartesian coordinate system (x, y, z) on flux form is:

$$\frac{\partial U}{\partial t} + \frac{\partial}{\partial x}\left(\frac{U^2}{H}\right) + \frac{\partial}{\partial y}\left(\frac{UV}{H}\right) - fV = -gH\frac{\partial \eta}{\partial x} - \frac{\tau_x^b}{\rho} \tag{4.10}$$

and

$$\frac{\partial V}{\partial t} + \frac{\partial}{\partial y}\left(\frac{V^2}{H}\right) + \frac{\partial}{\partial x}\left(\frac{UV}{H}\right) + fU = -gH\frac{\partial \eta}{\partial y} - \frac{\tau_y^b}{\rho} \tag{4.11}$$

[Moe et al., 2002]. Here η is the vertical displacement of the sea surface from the mean sea level H_0 and $H = H_0 + \eta$ is total depth, g is the acceleration of gravity and f the Coriolis parameter while τ_x^b and τ_y^b the bottom friction in u and v direction. The bottom friction is dependent on the squared of the velocities, and is parameterized in the following way

$$\boldsymbol{\tau}_x^b = \rho\, c_D \frac{\sqrt{U^2 + V^2}}{H}\frac{U}{H}, \qquad \boldsymbol{\tau}_y^b = \rho\, c_D \frac{\sqrt{U^2 + V^2}}{H}\frac{V}{H} \tag{4.12}$$

where c_D is the drag coefficient of the quadratic bottom shear stress. The relation between (U,V) which are the components of column flux vector per unit length in the horizontal plane, and the depth mean current velocity is

$$\bar{u} = \frac{U}{H}, \qquad \bar{v} = \frac{V}{H}. \tag{4.13}$$

The continuity equation using this notation then becomes

$$\frac{\partial \eta}{\partial t} = -\frac{\partial U}{\partial x} - \frac{\partial V}{\partial y}. \tag{4.14}$$

Finite volume method (FVM)

Given a domain of interest, the first step in the FVM approach is to divide the domain into a number of control volumes often refereed to as cells, forming a grid. Variables of interest should be located and calculated in the centroid of each cell. An advantage with FVM is that both structured and unstructured grids can be used. The difference between the two is best illustrated using Figure 4.1. The left grid is a structured grid while the right one is an unstructured grid.
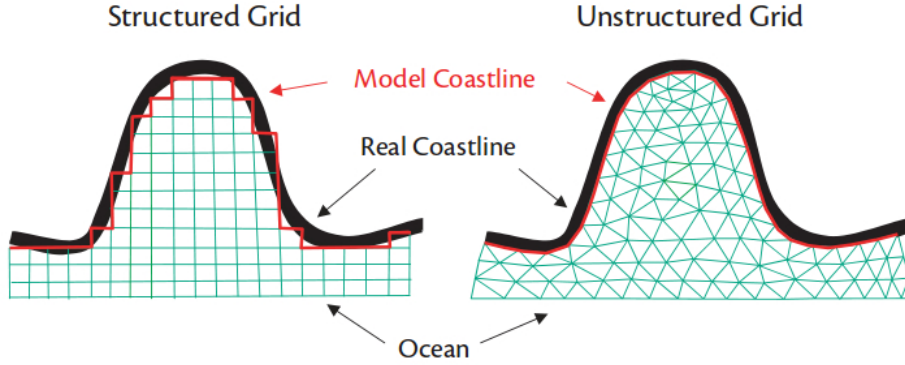

Figure 4.1: Illustration of structured vs unstructured grid. From [CHEN et al., 2006]

The unstructured grid provides higher accuracy and better modeling convergence. The downside is that the cell connectivity(number of connections for each cell and connected node numbers) must be specified. This means that a unstructured grid is more work and more complex to implement compared to the structured grid, but as the model becomes more precise it is generally worth it, especially for detailed coastlines where good resolution is needed. To obtain the discrete versions of the partial differential equations, control volume integration must be done. As the equations contain a divergence term, using Gauss' divergence theorem they are converted to surface integrals before they are evaluated as fluxes on the surface of each cell. To illustrate this, consider the following two dimensional example of a structured grid illustrated in Figure 4.2 from [Tu et al., 2013]. To approximate the first order derivative of Φ, the divergence theorem is applied

$$\left(\frac{\partial \Phi}{\partial x}\right) = \frac{1}{\Delta V} \int_V \frac{\partial \Phi}{\partial x} dV = \frac{1}{\Delta V} \int_A \Phi dA^x \approx \frac{1}{\Delta V} \sum_{i=1}^N \phi_i A_i^x \qquad (4.15)$$

N is the number of bounding surfaces and Φ_i represents variable values at each surface element. The same can also be applied to y-direction, as well as for the second order derivative. For the case illustrated in Figure 4.2, the first order approximation for x-direction becomes:

$$\frac{1}{\Delta V} \sum_{i_1}^N u_i A_i^x = \frac{1}{\Delta V}(u_e A_e^x - u_w A_w^x + u_n A_n^x - u_s A_s^x) =$$

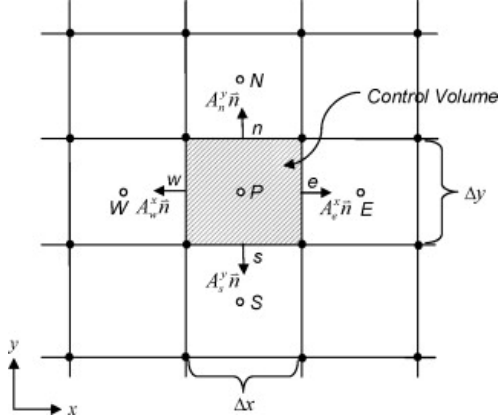$$\frac{1}{\Delta V}(u_e A_e^x - u_w A_w^x) \qquad (4.16)$$

19

Figure 4.2: Structured mesh example, from [Tu et al., 2013]

and similar for y-direction

$$\frac{1}{\Delta V}\sum_{i_1}^{N}v_iA_i^x = \frac{1}{\Delta V}(v_eA_e^x - v_wA_w^x + v_nA_n^x - v_sA_s^x) =$$

$$\frac{1}{\Delta V}(v_eA_e^x - v_wA_w^x) \tag{4.17}$$

u_e, u_w, v_n and v_s are located at the borders between the cells, so they can be found by simply taking the mean of the cell at each side

$$u_e = \frac{u_P + u_E}{2}, \quad v_n = \frac{v_P + v_N}{2} \quad \text{etc.} \tag{4.18}$$

In this case where the grid is uniform, $A_e^x = A_w^x = \Delta y$ and $A_s^y = A_n^y = \Delta x$, so the last step in expressing the discretization of the continuity equation in 2-D is

$$\frac{u_E - u_W}{2\Delta x} + \frac{v_N - v_S}{2\Delta y} = 0 \tag{4.19}$$

and this equation expresses the exact conservation of the relevant property for each control volume. This method combines the best of finite-difference method [Blumberg and Mellor, 1987] [Haidvogel et al., 1991] for simpler discrete computational efficiency and finite element method [Naimie, 1996] [Lynch and Naimie, 1993] for the geometric flexibility [Chen et al., 2003].

Grid design

The grid in FVCOM is an unstructured grid comprised of triangular cells which are non-overlapping. Each triangle consist of three nodes, one in each corner and a centroid. At the nodes, the sea surface elevation is estimated and are based on the flux through the surrounding triangles, while the velocities are estimated in the centroid and are based on a net flux though the three sides of that triangle [Chen et al., 2003]. The bottom friction is also calculated at each centroid, and this is done for the x and y direction using the following equations:

$$\tau_{bx} = \rho k_0|\mathbf{V}|u \tag{4.20}$$

20

$$\tau_{by} = \rho k_0 |\mathbf{V}| v \qquad (4.21)$$

where k_0 is the drag coefficient, which for depths less than three meters is given the constant value $k_0 = 0.0027$, while for depths larger than three meters it is given as

$$k_0 = g \left(\frac{H^\alpha}{NN} \right)^{-2} \qquad (4.22)$$

where NN = 0.02 and α=0.166667. Figure 4.3 shows how the friction is dependent on the depth. The continuity equation is solved over the area enclosed by the centroids surrounding each node
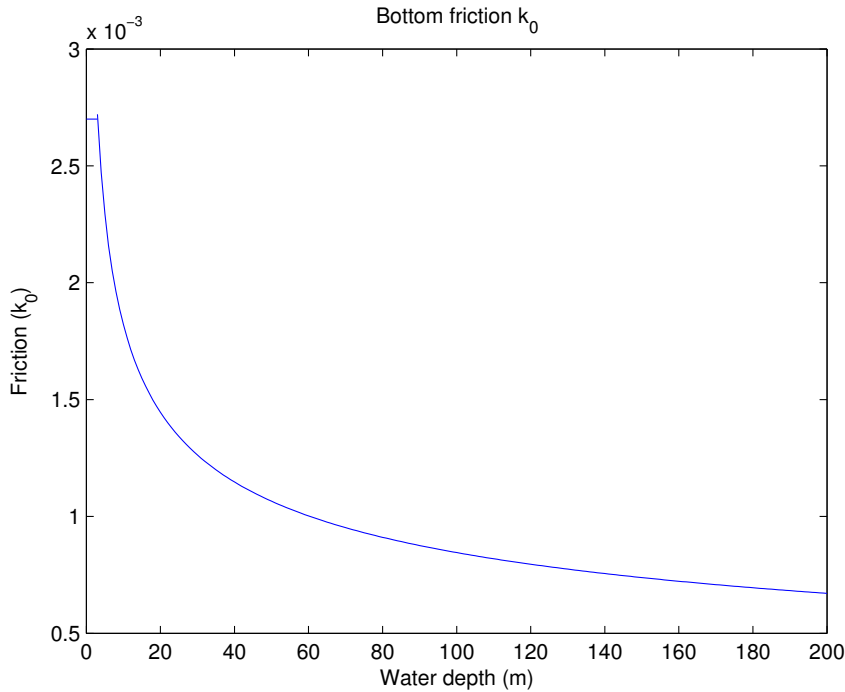

Figure 4.3: How bottom friction changes with water depth.

through fourth-order Runge-Kutta time-stepping scheme with second order accuracy [Dick, 1992]. The momentum on the other hand, is solved within each triangular cell, but using the same fourth-order Runge-Kutta method [Chen et al., 2003]. The equations are solved at every 0.5 second in the finer Troms-grid, while in the coarser NN-grid they are solved every 2.0 seconds. The results are saved every 15 minute. The equations must be solved at a higher frequency in the finer grid to be sure that the wave is detected within each cell. As the wave generally travels at the speed $v = \sqrt{gh}$, the smaller the cell and the deeper mean depth, the more frequent the equations must be solved to not miss out on any important contributions from any cell. As the resolution is coarse out in the open ocean where the depth is large, this is not where the issues arises, but when the resolution is really fine in areas with complex geometries and strong currents. Below is the resolution for the two grids shown, as well as the depth along the coast.
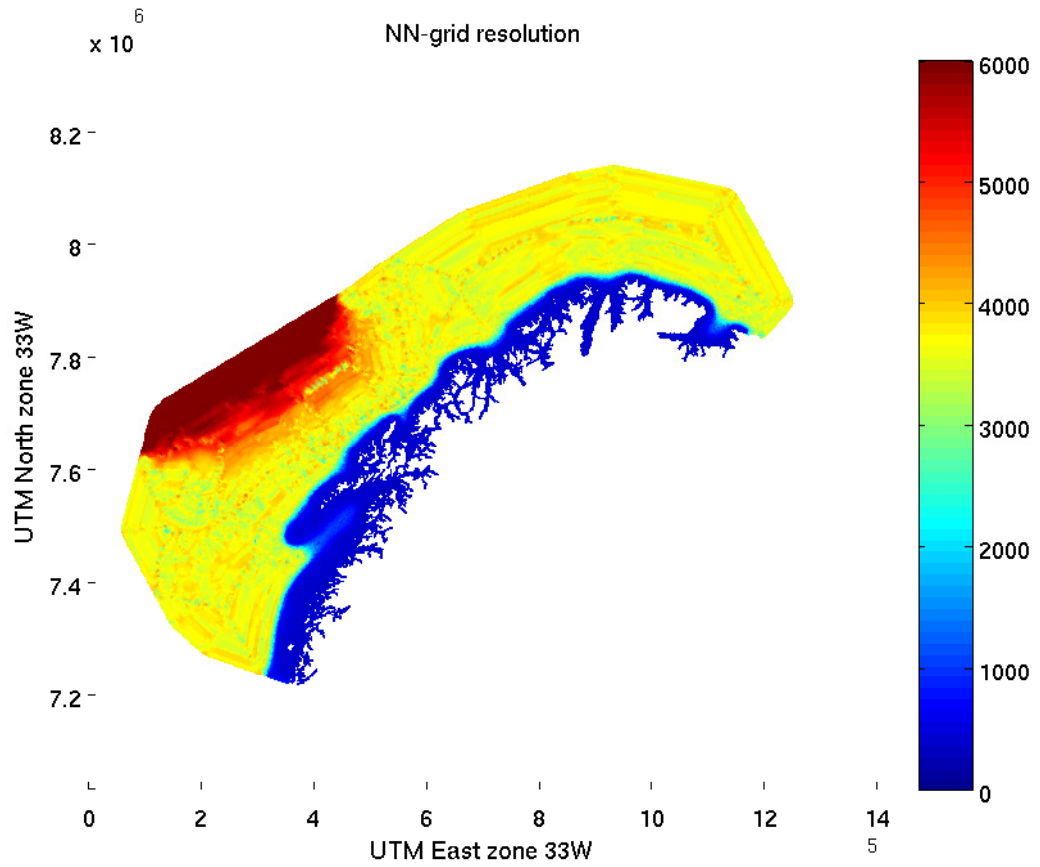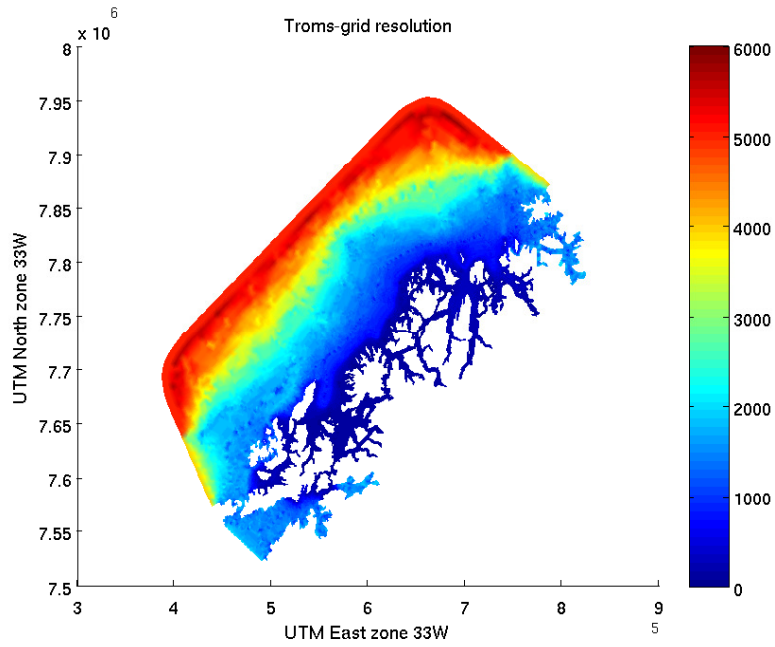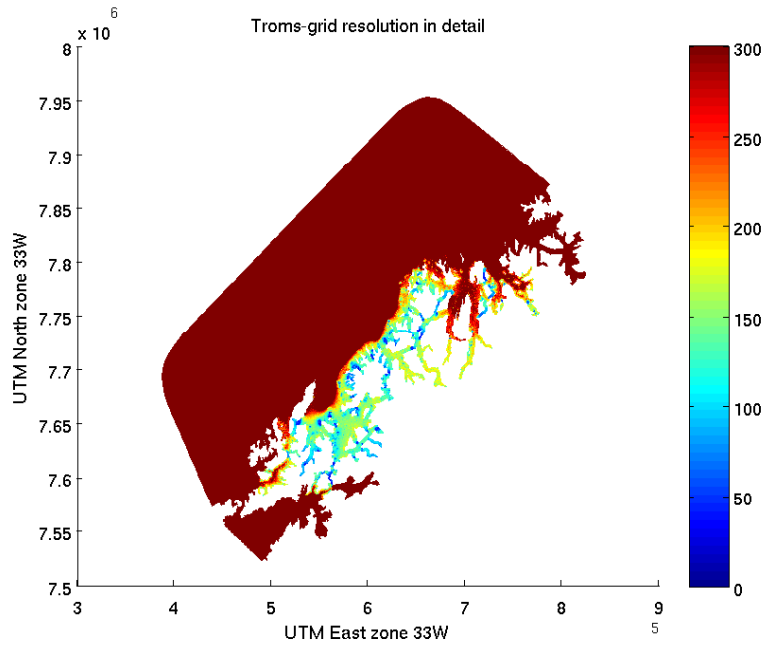
21

Figure 4.4: The resolution of the NN-grid. Along the coast it is approximately 500m. The colorbar is meters

(a) Troms-grid crude resolution. The colorbar is in(m)

(b) Troms-grid detailed resolution. The colorbar is in(m)

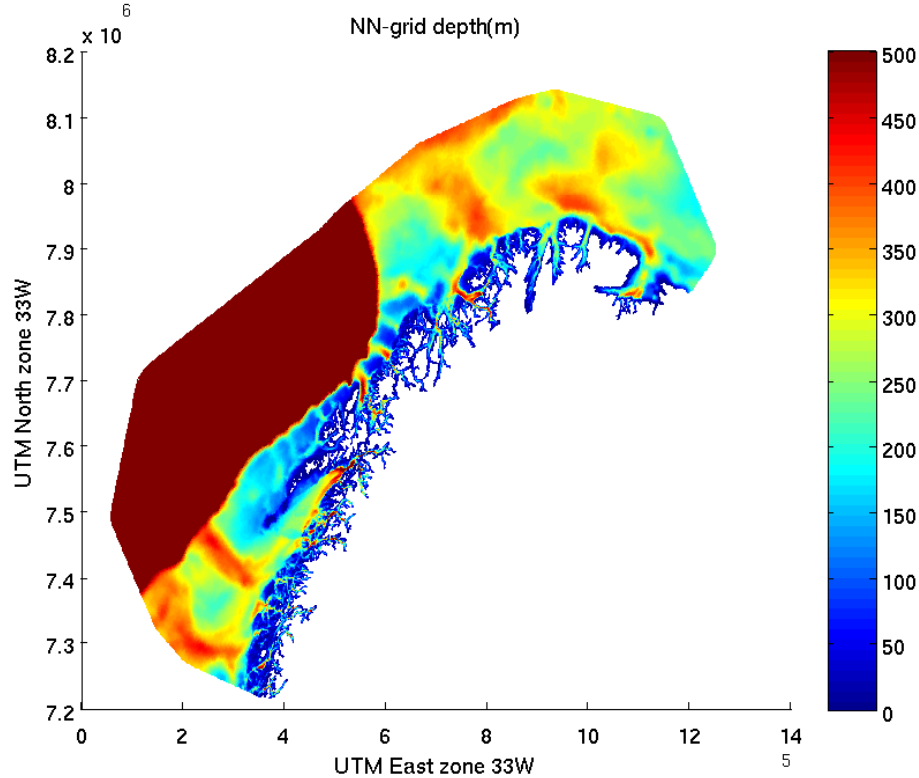Figure 4.5: Troms-grid resolution

23

Figure 4.6: Ocean depth along the North Norwegian coast. The colorbar is in(m)

Boundary condition

The initial condition of the model is zero velocity and zero surface elevation. The tide on the boundary is specified, and is gradually introduced over the course of the first 10 of the 100 days simulated. The physical forcing of the model is in the boundary conditions. To illustrate this, think of a rope on the ground, if the rope is being moved rapidly back and fourth, wave motions which propagates towards the end of the rope will appear. The area the model covers can be thought of as just a small part in the middle of the rope. In this run, the model simulates the eight major tidal constituent: M_2, N_2, S_2, K_2, K_1, O_1, P_1 and Q_1 which are explained in section 3.1. As discussed earlier in chapter 3, the tide has close to zero <u>local</u> effect, as can be seen in lakes where the tide causes the water height to vary only a few centimeters. This is why the boundary input is critical for a realistic simulation. The initial phase and amplitude of the tide wave is for the entire boundary taken from another model, named AOTIM [Padman and Erofeeva, 2004], which is an ocean model covering the arctic. Open boundary conditions for currents are not required in FVCOM, as they are located at the center of each triangular cell and are calculated with the assumption of mass conservation in the open boundary cell [Chen et al., 2003] . In addition, a sponge layer [Chen et al., 2013] is introduced, which is a damping zone acting within a prescribed radius from the boundary.

This sponge layer damps high frequency noise in the form of reflected waves which are generated in the model domain. It is important that these waves are not reflected back into the domain as they reach the boundary to minimize the error and thus maintaining proper realistic results throughout the model domain. The constituent boundary conditions can be seen in Figure 4.7. Even though P_1 and Q_1 are included among the 8 most significant tidal constituents, it becomes evident that the contribution from P_1 and Q_1 are not significant in the bigger picture.
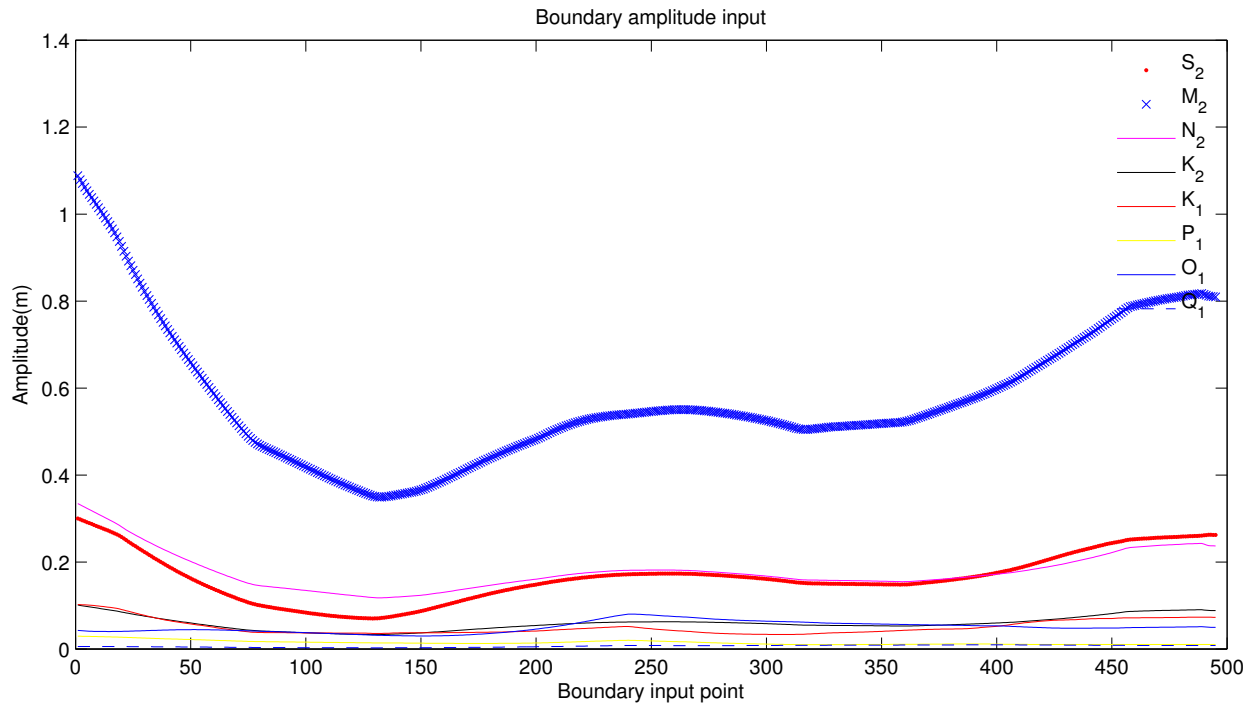

Figure 4.7: Amplitude at the boundary for the NN-grid.

Chapter 5

Tidal data analysis

In this chapter, results from tidal analysis will be represented. Data from the model as well as measurement data will be analyzed with the goal to determine the accuracy of the model. The analysis is done using Utide described in section 3.1.1. A test was performed on a dataset provided by Sjøkartverket to check if using Utide resulted in the same analysis results as Sjøkartverkets analysis tools did. As seen in Table 5.1 below, the analysis is in almost complete agreement.

Constituent	Utide Amplitude [cm]	Sjøkartverket amplitude [cm]
M_2	72.4	72.4
S_2	23.7	23.7
N_2	15	15.1
K_2	6.8	6.8
K_1	7	7
P_1	1.9	2.1
Q_1	2.2	2.2
O_1	3.9	3.8

Table 5.1: Utide validation

Grid-setup

In the validation process, two grids as seen on Figure 5.1 where analyzed. One grid covers the entire Northern-Norway, called the NN-grid. This grid is rather coarse in its resolution, and along the coast the resolution is 500 meters as seen on Figure 4.6 and consists of 339036 cells. The other grid, covering Troms county is a high resolution grid with more cells than the NN-grid at 392669 cells with resolution seen on Figure 4.5, even though it is approximately three times smaller.
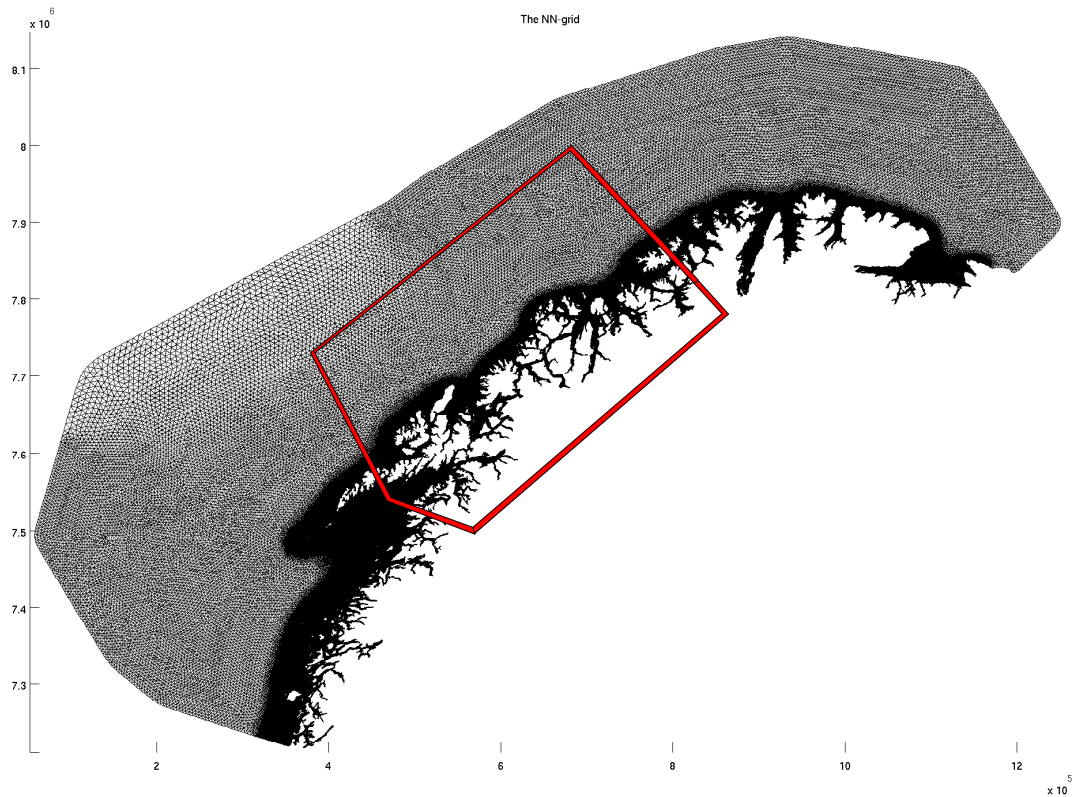

Figure 5.1: The whole figure represent the Northern-Norway grid(NN-grid). The red box illustrates the Troms-grid

5.0.1   The pressure data set

Pressure data analysis

The database used consists of data from about 1995-2014, but the earlier records where done with instruments of to low accuracy for this purpose. Datasets covering 19 locations with good pressure-data was analyzed to study the tides characteristics along the coast in Troms county using the

Troms-grid, but also using the entire NN-grid to see how the two compare. Even if the datasets have data which looks good, it is important to keep in mind that for most of the locations the measurements are recorded, are with regard to analyzing fish-farm locations, and are not placed at such a location as to get the best possible data for tidal analysis.

The comparison of the amplitude for constituents M_2, S_2, K_1 and O_1 for the 19 locations studied is represented in Tables 5.2, 5.3, 5.4 and 5.5 respectively, with a Figure below to visualize the amplitude difference It is worth noting that location 1, 5, 8 and 10 are all close to the boundary with respect to the Troms-grid model domain. See Figure 5.2 for a location map.
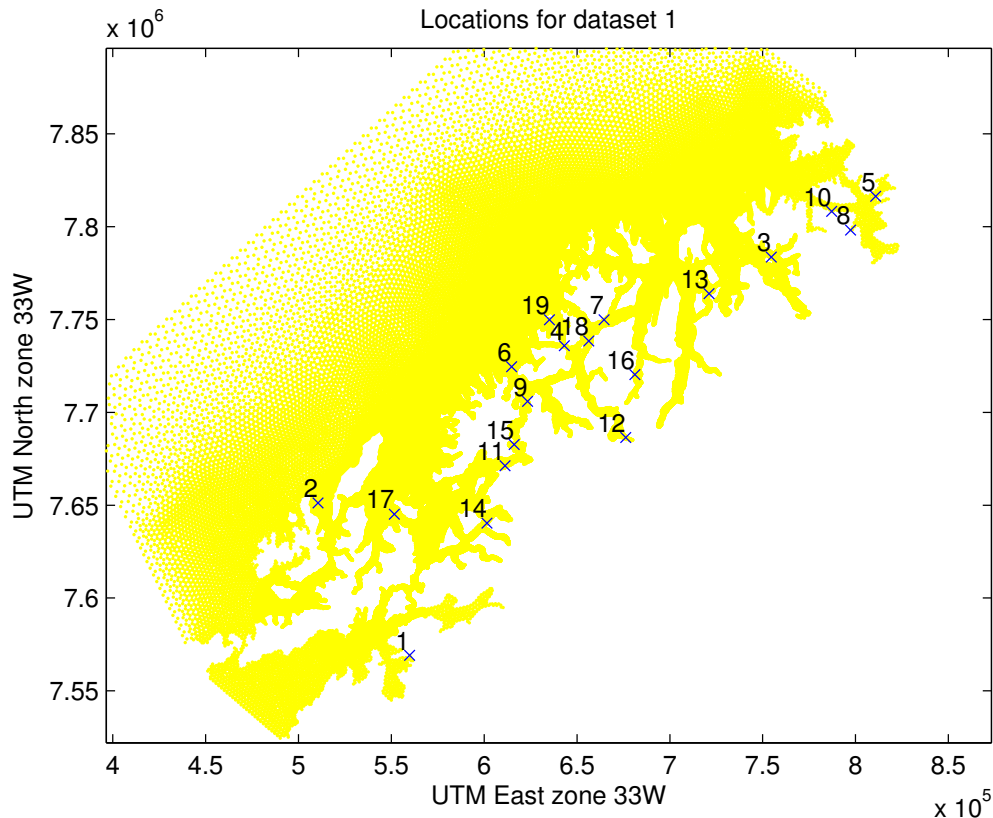

Figure 5.2: Troms-grid with location 1-19.

In Chapter 1, Figure 1.1 the overall amplitude of the tide along the Norwegian coast is shown. To check if the measured data matches this, the M_2 amplitude have been plotted in order of increasing longitude, and in order of increasing amplitude. Figure 1.1 and 5.3 are in good agreement, and show that the amplitude increase northeastwards. This is also confirmed in [Gjevik, 2009]. The reason for an agreement which is not perfect between the amplitude order and longitude order might come from the fact that for shallow locations close to the shore, the amplitude is generally higher than for areas where the water depth is large.
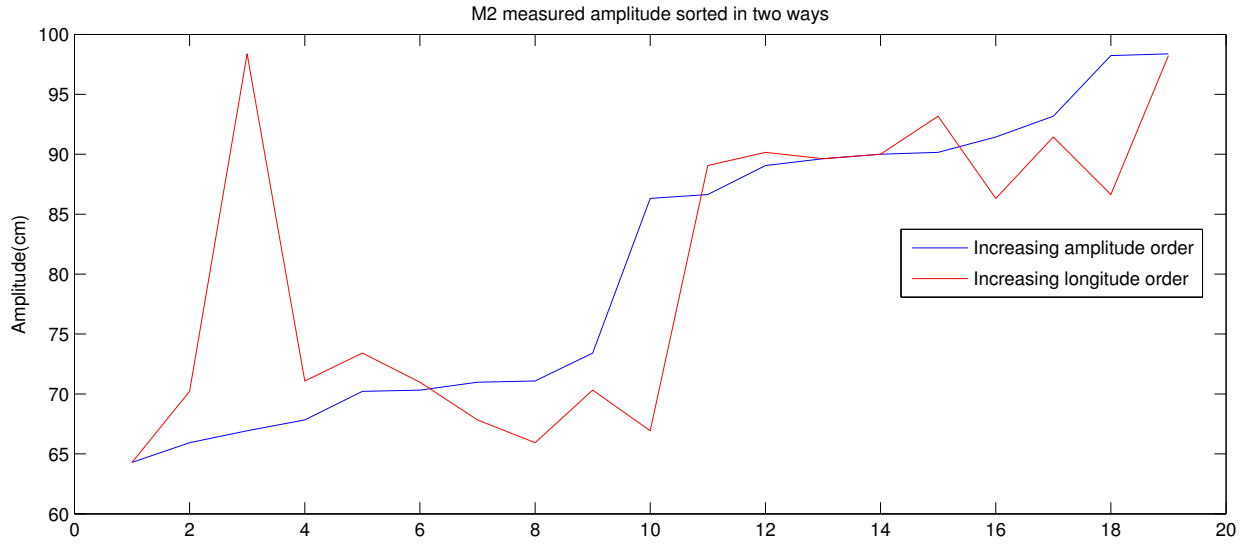
Figure 5.3: Locations 1-19 sorted in increasing amplitude and increasing longitude

Location	$\mathbf{A_M} M_2$ (cm)	$\mathbf{A_T} M_2$ (cm)	$\mathbf{A_{NN}} M_2$ (cm)	$\mathbf{P_M} M_2$ (degree)	$\mathbf{P_T} M_2$ (degree)	$\mathbf{P_{NN}} M_2$ (degree)
(1) Efjord	98.37	88.24	96.41	343.08	332.36	313.44
(2) Gisøya	64.29	61.67	62.95	330.94	315.35	317.20
(3) Jokelfjord 2	86.32	85.69	86.28	357.52	337.55	339.69
(4) Kaldfjord	66.93	68.91	67.85	333.95	319.35	319.24
(5) Kråkevika	98.23	90.00	86.80	1.52	342.52	346.92
(6) Kvalen	67.83	67.04	65.92	38.55	319.55	319.81
(7) Laksklubb bukta	90.16	83.91	85.55	348.22	333.77	335.80
(8) Langfjorden	86.64	88.83	87.26	2.39	342.22	346.33
(9) Lenvika	65.93	68.49	67.25	339.30	319.36	319.63
(10) Lokkarfjord	91.45	88.83	85.71	1.27	342.22	345.80
(11) Mohamna	73.41	68.38	67.75	330.07	318.68	319.48
(12) Nordkjosbotn	89.62	83.07	85.67	55.98	330.59	337.80
(13) Russelv	93.17	85.73	86.62	349.74	335.06	336.87
(14) Salaks	71.09	68.56	67.80	333.14	318.81	319.39
(15) Silsand	70.98	69.03	68.33	11.73	318.88	319.66
(16) Sjursnes	90.01	87.02	88.71	358.99	339.47	339.60
(17) Toppsund	70.22	66.43	65.94	325.19	317.96	318.89
(18) Tromsøysundet	89.05	82.96	85.35	354.10	333.24	335.62
(19) Vengsøya	70.32	68.43	67.40	333.33	319.43	319.34

Table 5.2: M_2 amplitude and phaselag using the two grids. A=amplitude, P=Phase, while $_{M,T}$ and $_{NN}$ represents data from measurements, Troms-grid and Northern-Norway grid respectively
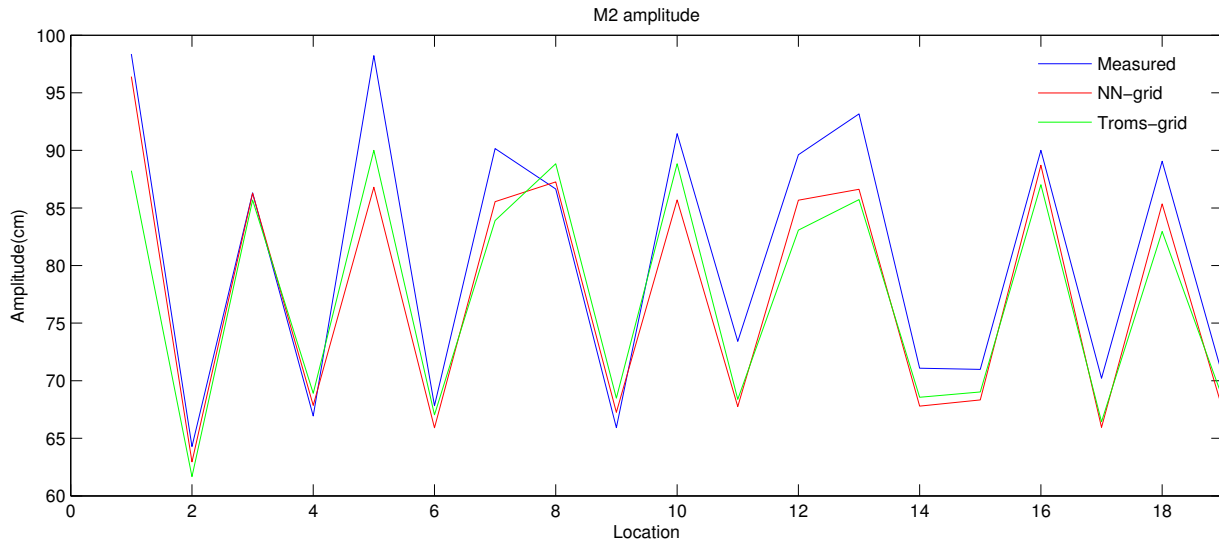

Figure 5.4: M_2 amplitude from Table 5.2 illustrated

Location	$\mathbf{A_M}S_2$ (cm)	$\mathbf{A_T}S_2$ (cm)	$\mathbf{A_{NN}}S_2$ (cm)	$\mathbf{P_M}S_2$ (degree)	$\mathbf{P_T}S_2$ (degree)	$\mathbf{P_{NN}}S_2$ (degree)
(1) Efjord	29.51	32.28	29.23	19.45	18.18	4.34
(2) Gisøya	28.27	19.92	19.97	1.71	6.99	7.47
(3) Jokelfjord 2	14.69	28.21	26.43	89.90	27.89	30.90
(4) Kaldfjord	25.64	21.52	21.71	6.66	10.34	10.06
(5) Kråkevika	29.26	29.17	26.08	37.33	32.77	37.80
(6) Kvalen	10.41	21.06	21.07	62.70	10.50	10.13
(7) Laksklubb bukta	32.35	27.80	26.66	39.47	24.00	26.80
(8) Langfjorden	26.23	28.83	26.27	27.34	32.48	37.19
(9) Lenvika	18.95	21.54	21.46	29.28	10.29	9.96
(10) Lokkarfjord	26.09	28.83	25.80	26.70	32.48	36.67
(11) Mohamna	23.93	21.78	21.59	353.80	9.79	9.67
(12) Nordkjosbotn	22.15	26.87	27.62	110.22	21.99	29.67
(13) Russelv	27.20	28.28	26.76	42.63	25.34	28.09
(14) Salaks	21.92	21.87	21.60	8.54	9.93	9.61
(15) Silsand	24.13	21.99	21.77	38.64	9.98	9.86
(16) Sjursnes	14.97	28.98	27.56	18.28	31.38	31.97
(17) Toppsund	34.88	21.12	21.04	6.31	9.07	9.04
(18) Tromsøysundet	23.22	27.52	26.75	0.52	23.55	26.53
(19) Vengsøya	28.13	21.38	21.57	350.81	10.41	10.12

Table 5.3: S_2 amplitude and phaselag using the two grids. A=amplitude, P=Phase, while $_{M,T}$ and $_{NN}$ represents data from measurements, Troms-grid and Northern-Norway grid respectively
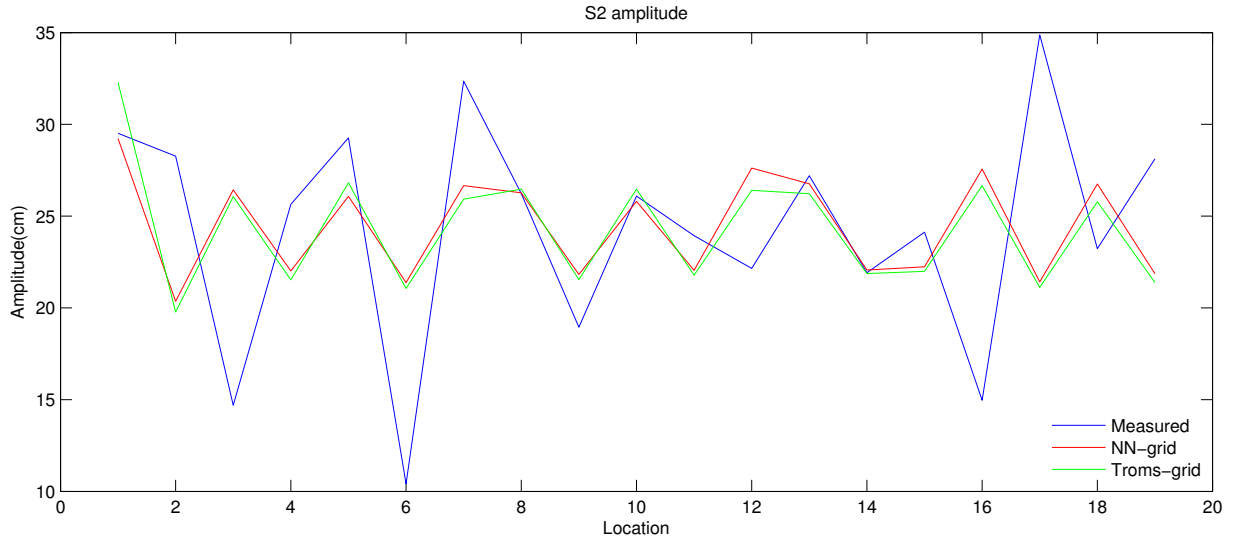

Figure 5.5: M_2 amplitude from Table 5.3 illustrated

Location	$\mathbf{A_M}K_1$ (cm)	$\mathbf{A_T}K_1$ (cm)	$\mathbf{A_{NN}}K_1$ (cm)	$\mathbf{P_M}K_1$ (degree)	$\mathbf{P_T}K_1$ (degree)	$\mathbf{P_{NN}}K_1$ (degree)
(1) Efjord	15.09	11.36	10.46	82.43	83.78	85.43
(2) Gisøya	4.43	6.88	9.16	94.82	80.82	220.07
(3) Jokelfjord 2	11.84	8.30	8.40	78.95	68.85	88.17
(4) Kaldfjord	8.56	7.87	8.33	83.35	74.84	81.85
(5) Kråkevika	10.61	8.12	8.47	91.61	73.96	89.90
(6) Kvalen	8.06	7.82	8.23	100.15	75.05	82.55
(7) Laksklubb bukta	10.24	8.35	8.49	82.37	69.17	87.10
(8) Langfjorden	6.65	8.10	8.46	66.01	73.78	89.75
(9) Lenvika	8.79	7.85	8.26	82.76	74.80	82.24
(10) Lokkarfjord	8.00	8.10	8.41	59.10	73.78	89.55
(11) Mohamna	3.19	7.84	8.23	75.51	71.52	73.28
(12) Nordkjosbotn	8.79	8.29	8.75	116.01	76.39	90.12
(13) Russelv	8.84	8.37	8.44	92.80	68.14	87.33
(14) Salaks	2.07	7.85	8.23	173.00	71.36	73.05
(15) Silsand	6.07	7.84	8.25	82.74	72.00	74.06
(16) Sjursnes	8.56	8.53	8.55	77.19	72.78	90.07
(17) Toppsund	4.49	7.79	8.19	43.12	71.10	73.04
(18) Tromsøysundet	9.75	8.33	8.52	77.72	70.12	87.27
(19) Vengsøya	5.05	7.86	8.31	59.80	74.87	81.87

Table 5.4: K_1 amplitude and phaselag using the two grids. A=amplitude, P=Phase, while $_{M,T}$ and $_{NN}$ represents data from measurements, Troms-grid and Northern-Norway grid respectively
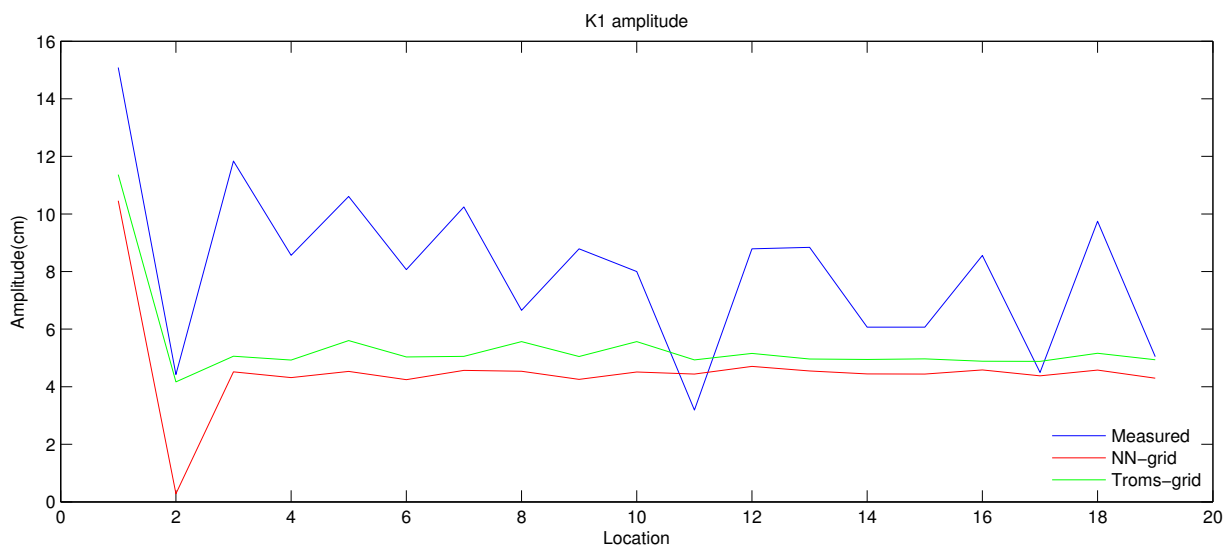

Figure 5.6: K_1 amplitude from Table 5.4 illustrated

33

Location	$\mathbf{A_M}O_1$ (cm)	$\mathbf{A_T}O_1$ (cm)	$\mathbf{A_{NN}}O_1$ (cm)	$\mathbf{P_M}O_1$ (degree)	$\mathbf{P_T}O_1$ (degree)	$\mathbf{P_{NN}}O_1$ (degree)
(1) Efjord	1.96	6.87	5.75	19.05	22.79	14.12
(2) Gisøya	2.88	4.17	1.45	45.83	18.15	1.31
(3) Jokelfjord 2	7.37	5.06	4.52	28.94	21.54	15.51
(4) Kaldfjord	2.42	4.93	4.31	49.61	18.09	12.38
(5) Kråkevika	2.07	5.60	4.53	43.66	23.82	17.73
(6) Kvalen	3.53	5.03	4.24	58.64	17.93	11.31
(7) Laksklubb bukta	3.68	5.05	4.57	57.06	20.28	14.29
(8) Langfjorden	4.28	5.57	4.54	75.82	23.67	17.60
(9) Lenvika	6.89	5.05	4.25	27.70	17.74	11.17
(10) Lokkarfjord	4.63	5.57	4.51	50.37	23.67	17.49
(11) Mohamna	1.62	4.93	4.44	259.06	17.86	11.20
(12) Nordkjosbotn	3.36	5.16	4.70	66.50	22.02	16.85
(13) Russelv	4.23	4.96	4.55	36.11	20.90	14.75
(14) Salaks	7.71	4.95	4.44	238.03	17.89	11.20
(15) Silsand	4.56	4.97	4.44	73.48	17.78	11.25
(16) Sjursnes	2.98	4.89	4.58	41.19	24.14	17.32
(17) Toppsund	3.15	4.88	4.38	63.84	17.48	10.87
(18) Tromsøysundet	3.97	5.16	4.58	51.92	20.33	14.39
(19) Vengsøya	5.24	4.93	4.29	63.75	18.13	12.30

Table 5.5: O_1 amplitude and phaselag using the two grids. A=amplitude, P=Phase, while $_{M,T}$ and $_{NN}$ represents data from measurements, Troms-grid and Northern-Norway grid respectively
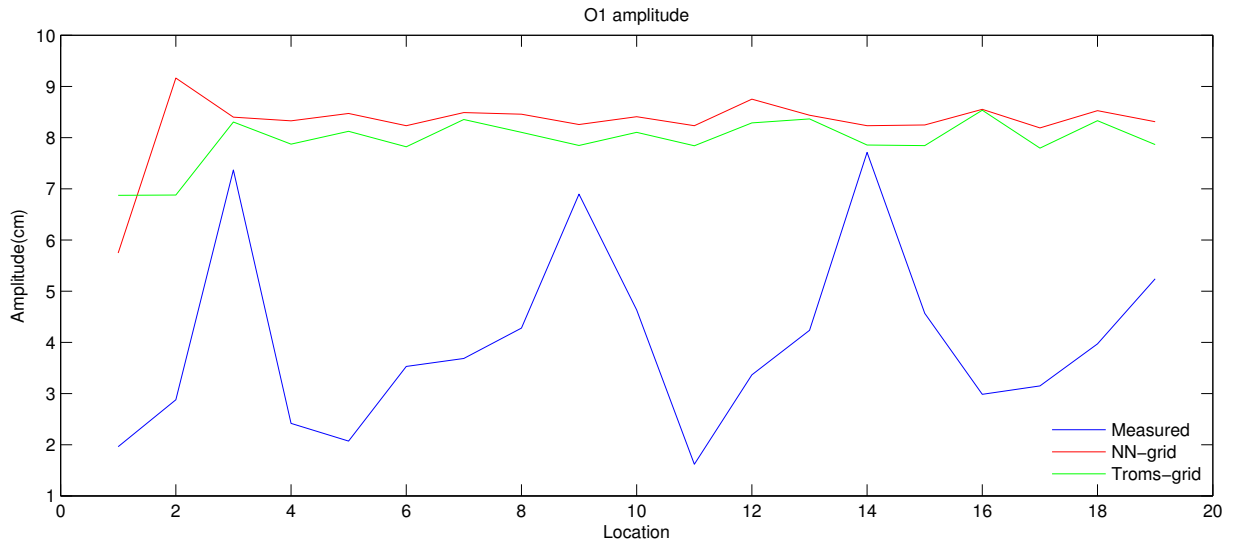

Figure 5.7: Amplitude from Table 5.5 illustrated

To illustrate the error from the measurements, the following equation is used

$$Error = 100 * |true - estimate|/true. \qquad (5.1)$$

The error is represented in Table 5.6 As the constituent amplitude decrease, the error increase.

Constituent	Troms-grid mean error	NN-grid mean error
M_2	5.04 %	4.35 %
S_2	27.11%	25.54 %
K_1	40.64 %	45.56 %
O_1	62.58 %	49.52%

Table 5.6: Model amplitude error

This is not as bad as it looks, as in general along the coast of Troms over 90% of all tidal height variations comes from the semidiurnal constituents, and M_2 is by far the biggest contributer.

There are other factors to discuss as well, besides the amplitude. The Greenwich phase lags are also computed in Table 5.2, 5.3, 5.4 and 5.5, and this gives an indication on how the tidal wave propagates, with values ranging from 0-360°. Greenwich phase lag is the phase lag of the constituent behind the Greenwich phase. Again it can been seen that M_2 is the constituent most accurately modeled. The phase difference is in general at a minimum for locations close to the open sea, and maximum within the deeper fjords, where the tidal wave has to pass complex terrain to reach. Following this general impression, location 6 should provide rather accurate model results as it is located close to the open sea, but this is not the case. There can be several reasons for this. The measurement data could be of bad quality because of an error on the instrument. The measuring instrument could also have been placed next to large boulder or in an underwater chasm. Another option is that the model somehow struggles in this area. However, as the results from the two different grids used are close to identical, and the correlation between measured and modeled data for the neighboring points are much higher it is probably the measured data which is corrupt.

Velocity data analysis

A common method for analyzing tidal velocity data is to look at tidal ellipses. Analyzing velocity data using Utide gives out the ellipse major and minor axis and the ellipse orientation angle θ. Knowing those three parameters, an ellipse can be drawn to illustrate the main directions of the water flow at any given point in the model, or for the observed locations. The following Figure 5.8 to 5.13 illustrates some of the locations with ellipse plots of the four most energetic tidal constituents.
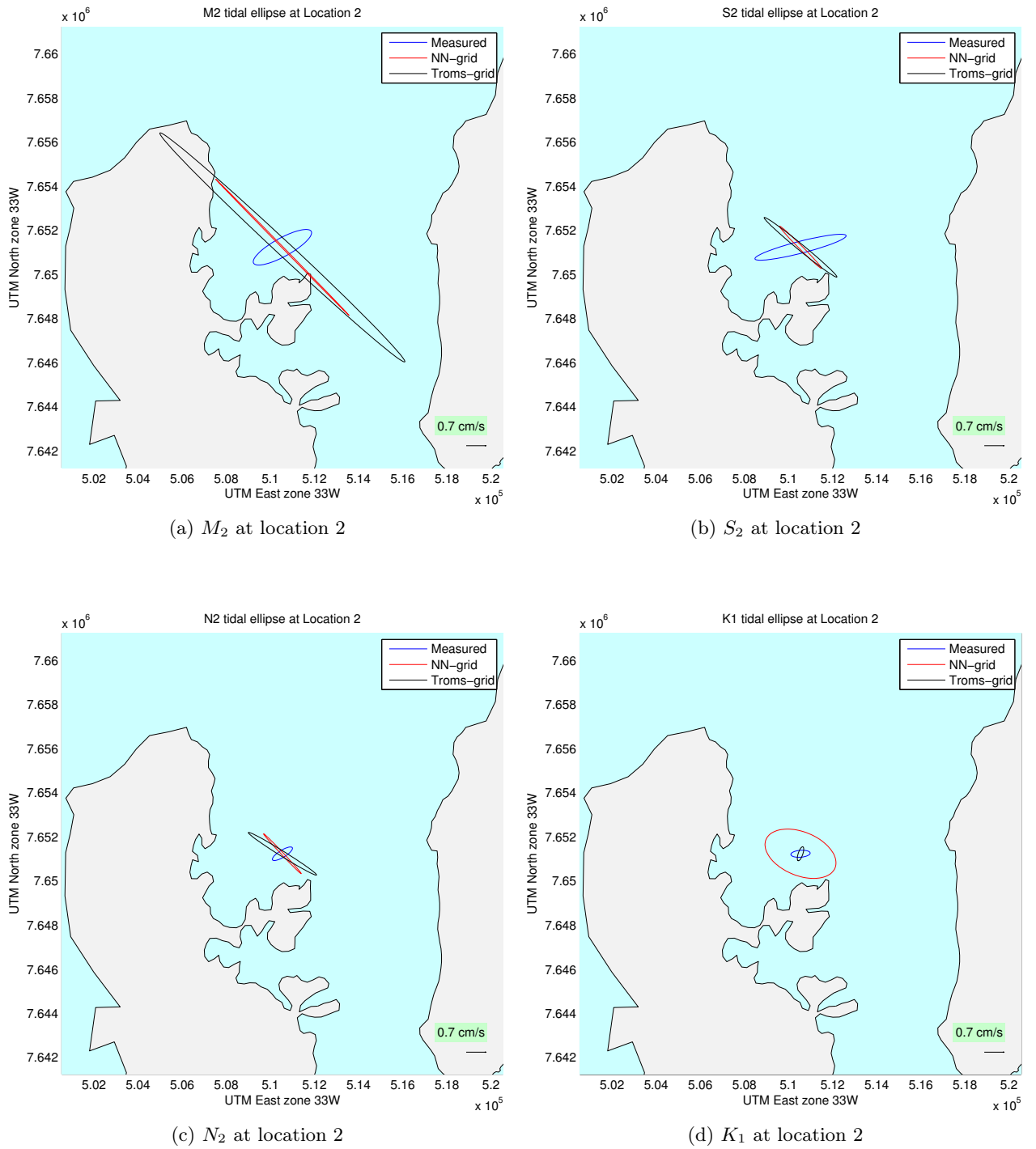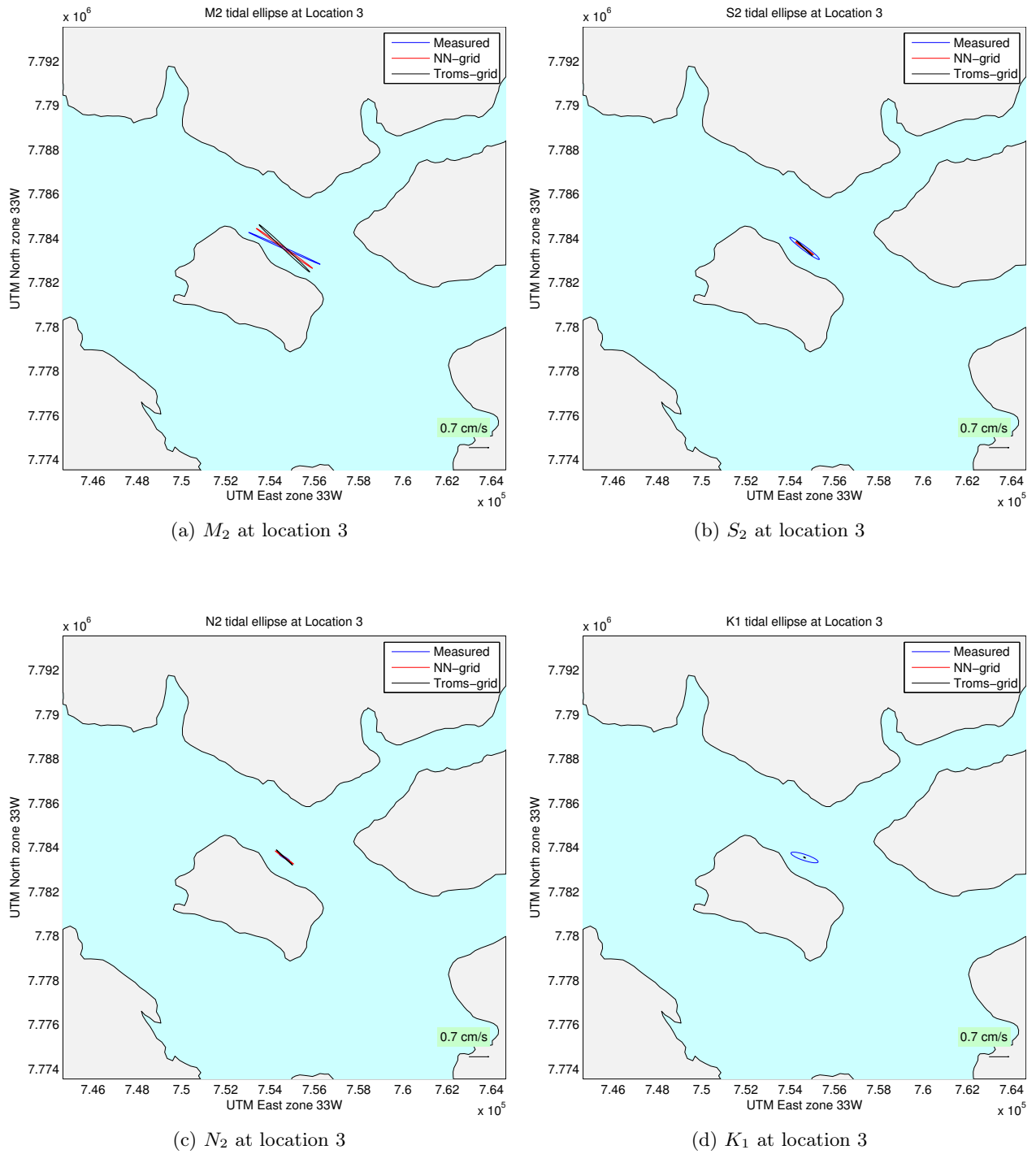
(a) M_2 at location 2

(b) S_2 at location 2

(c) N_2 at location 2

(d) K_1 at location 2

Figure 5.8: Troms-grid location 2

(a) M_2 at location 3

(b) S_2 at location 3

(c) N_2 at location 3

(d) K_1 at location 3

Figure 5.9: Tidal ellipses at location 3

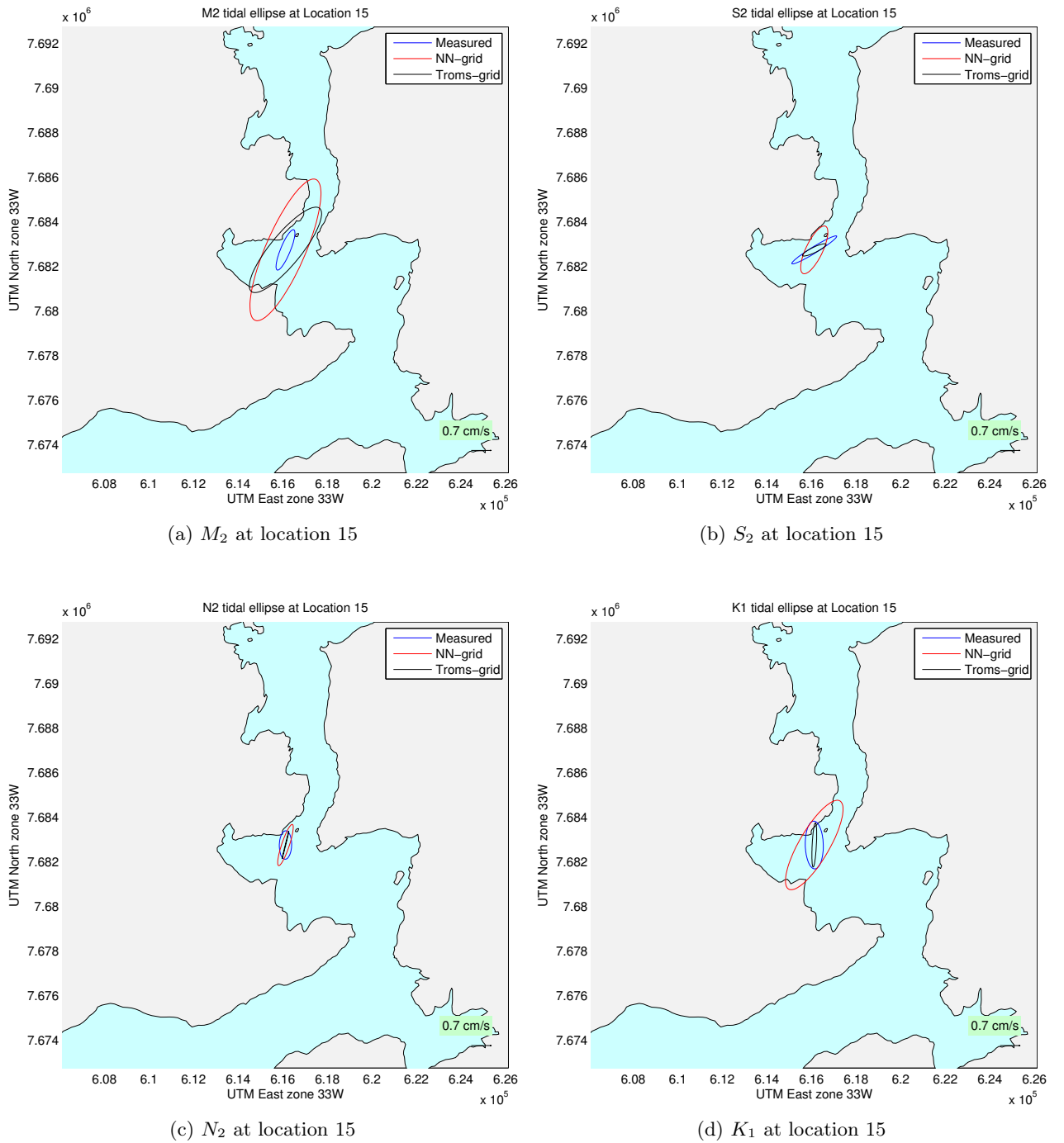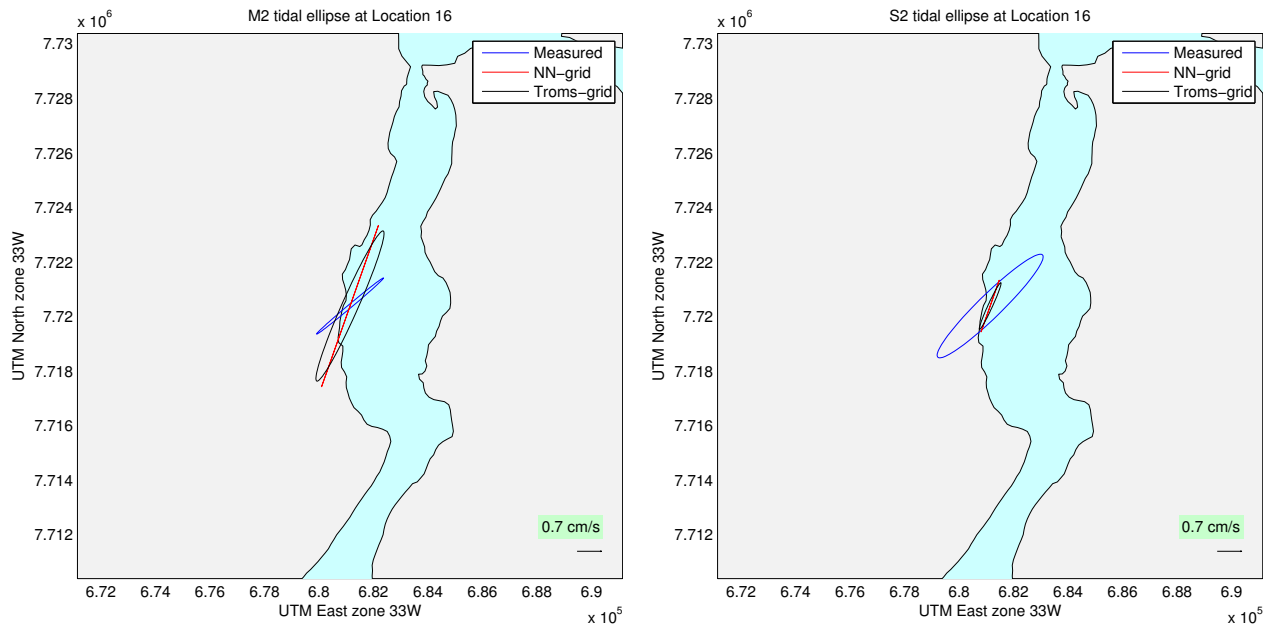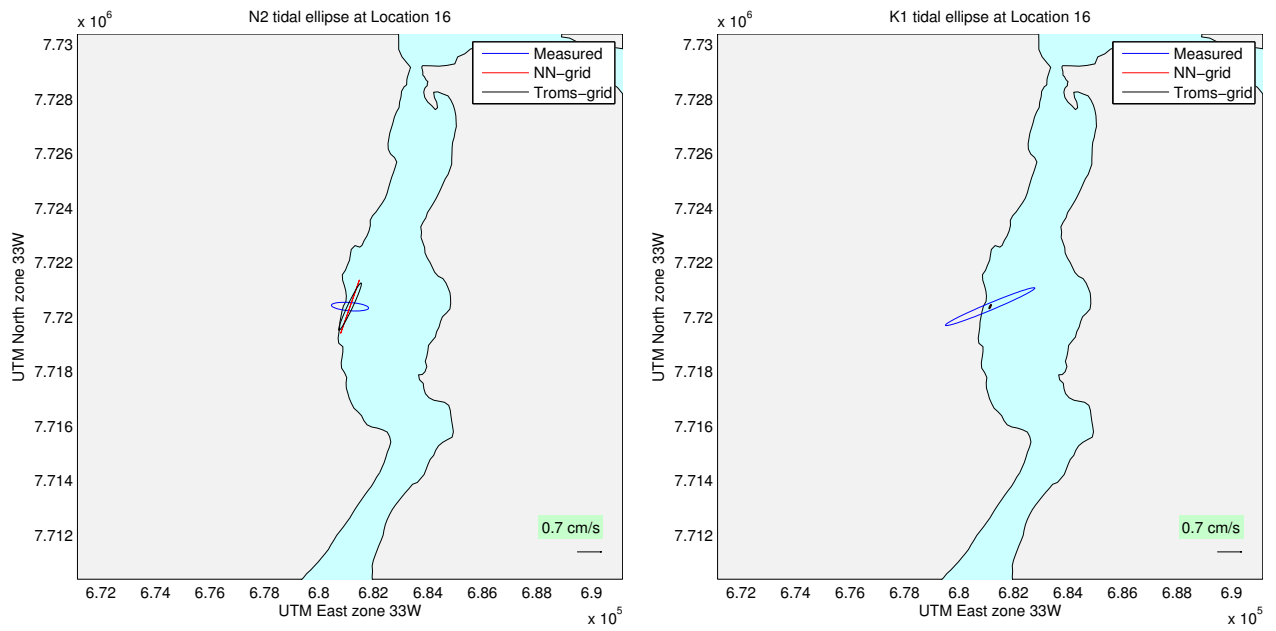(a) M_2 at location 9

(b) S_2 at location 9

(c) N_2 at location 9
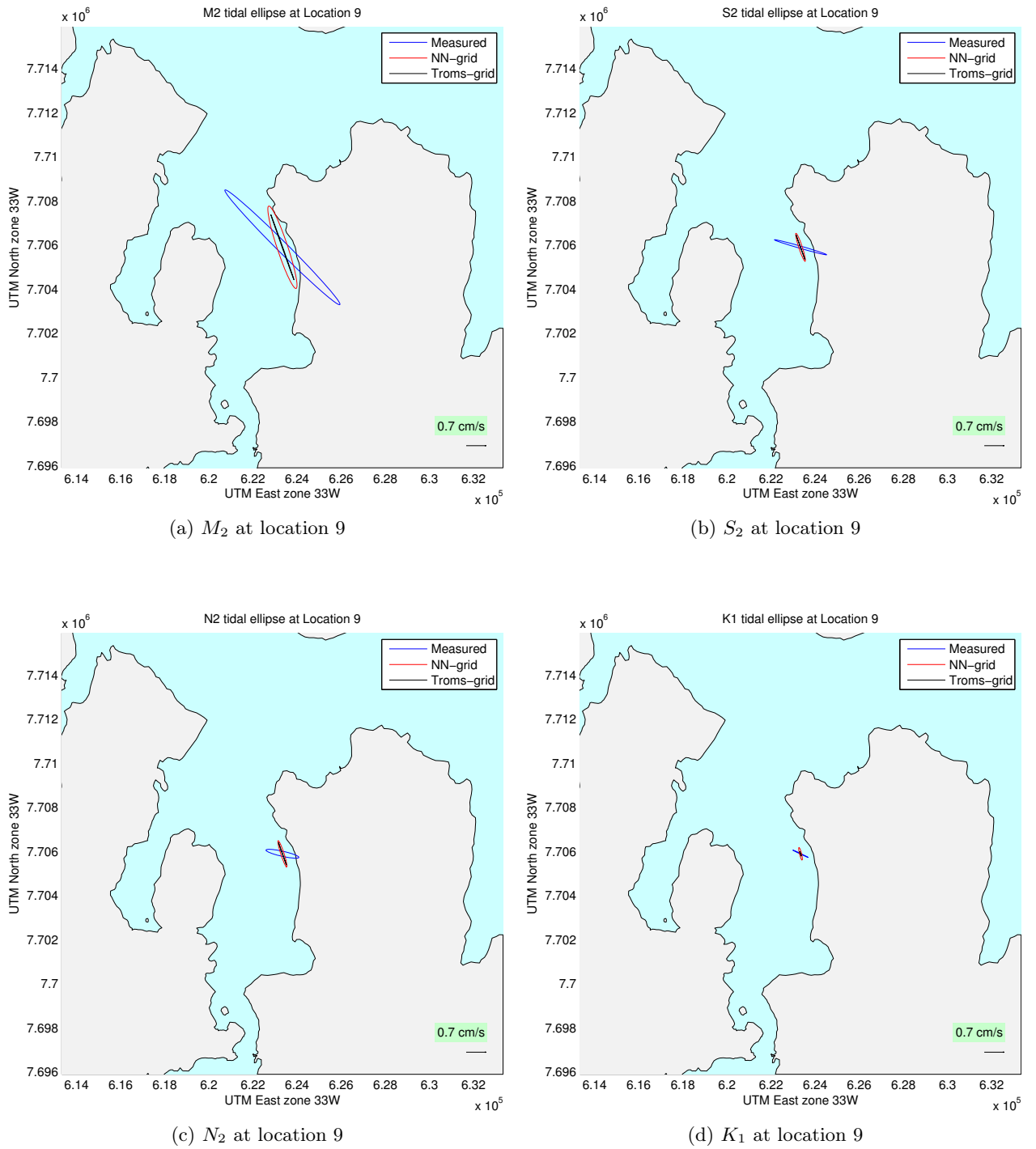
(d) K_1 at location 9

Figure 5.10: Tidal ellipses at location 9

38

(a) M_2 at location 10

(b) S_2 at location 10

(c) N_2 at location 10
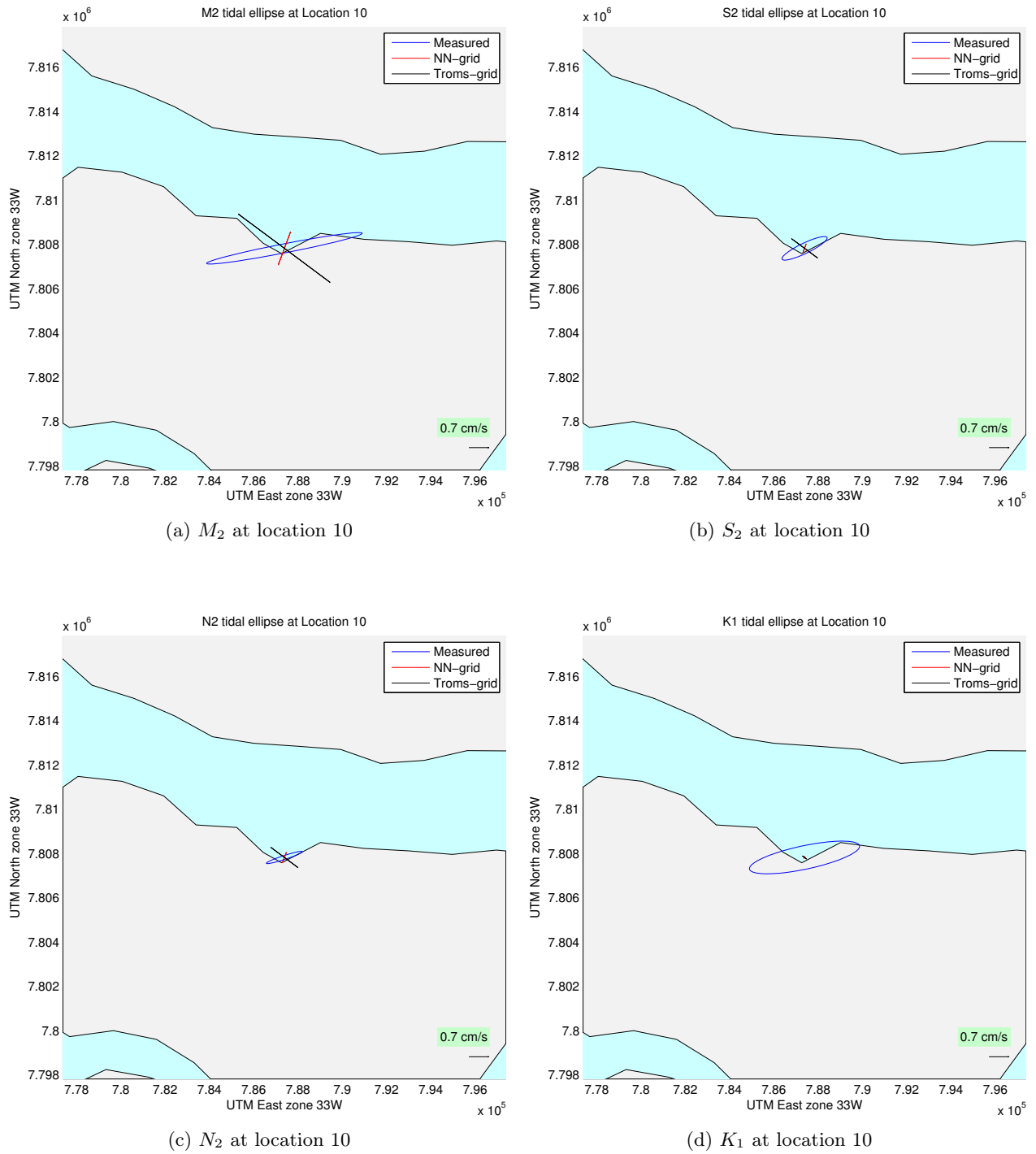
(d) K_1 at location 10

Figure 5.11: Tidal ellipses at location 10

(a) M_2 at location 15

(b) S_2 at location 15

(c) N_2 at location 15

(d) K_1 at location 15

Figure 5.12: Tidal ellipses at location 15

(a) M_2 at location 16

(b) S_2 at location 16

(c) N_2 at location 16

(d) K_1 at location 16

Figure 5.13: Tidal ellipses at location 16

41

On Figure 5.8 the agreement between the two modeled grids is quite good for M_2, S_2 and N_2. They do not agree with the measured results though, so the models struggles a bit in this area. For K_1 the finer Troms-grid does a better job for the amplitude of the velocity, while the NN-grid is closer with regards to direction.

For location 3 on Figure 5.9 both models does a good job. The NN-grid is slightly better than the Troms-grid, which is no surprise as this location is near the northern boundary of the Troms-grid, and from Figure 4.6 and 4.5 it can be seen that NN-grid has higher resolution in this area. For K_1 both models indicates that there is close to zero contribution, but the measured data indicates that the contribution from K_1 is on the same scale as N_2.

For location 9, it can be seen on Figure 5.10 that while the model results from both grids gives the logical results that the currents flow along the coastline, the measured results indicate that for the given location, the current is stronger and headed slightly towards the coastline. This seems illogical, but can be due to local abnormality in the topography, or even a compass error on the recording instrument.

The next location illustrated with tidal ellipses is location 10 on Figure 5.11. In this location, all three ellipses deviate from each other. While both grids struggle with this location, it is the finer Troms-grid which gives the results closest to the measured ones, and again K_1 is the constituent the modeling struggles the most with.

At location number 15 seen on Figure 5.12, both grids estimates to high velocities compared to the measured one. The Troms-grid is closest to the validation data, and at this location the model is better at modeling K_1 correctly than on previous locations.

Location 16 provides another good example where the two modeled results are in agreement with each other and indicates that the tidal current travel more along the coastline, while the measured results indicate the the current for the location is more towards the coastline. For K_1 however neither models register any significant contribution, but the measured results implies that the K_1 contribution is rather significant for the location.

Surprisingly, the data from the fine Troms-grid is generally not performing much better than the coarser NN-grid data. There can be several explanations for why this is the case. The biggest issue is the fact that for the 19 locations above discussed so far, the velocities measured are mainly from measurements done 3 meters above the ocean floor, while the model velocities are depth integrated, so they represent the average velocity for the entire depth of the location. Another possible source of error is that the locations used do not necessarily represent the average tidal effect in the area well. This is because the locations are mainly chosen to study properties relevant for a potential fish farm at the location, and not to get an impression of how the tide behaves in the area. The data can often be representative for the surrounding area, but not always. Another possible issue with the fine Troms-grid is that the boundary to the south is cutting off the Lofoten-islands, which is an area where the tidal wave is experiencing great change as seen on Figure 1.1. The Troms-grid also operates with a rather coarse resolution in the southernmost area of the domain close to the coast as seen in Figure 4.5. Altogether, this might provide the model with an error, and as the wave propagates northeastward along the coast, this error might also be propagated along to influence

the entire coastal area modeled.

To see if the modeled result tend to do better at high or low velocities, the major axis of the modeled ellipses have been plotted vs the measured equivalent. From Figure 5.14 it becomes clear

(a) M_2 major axis

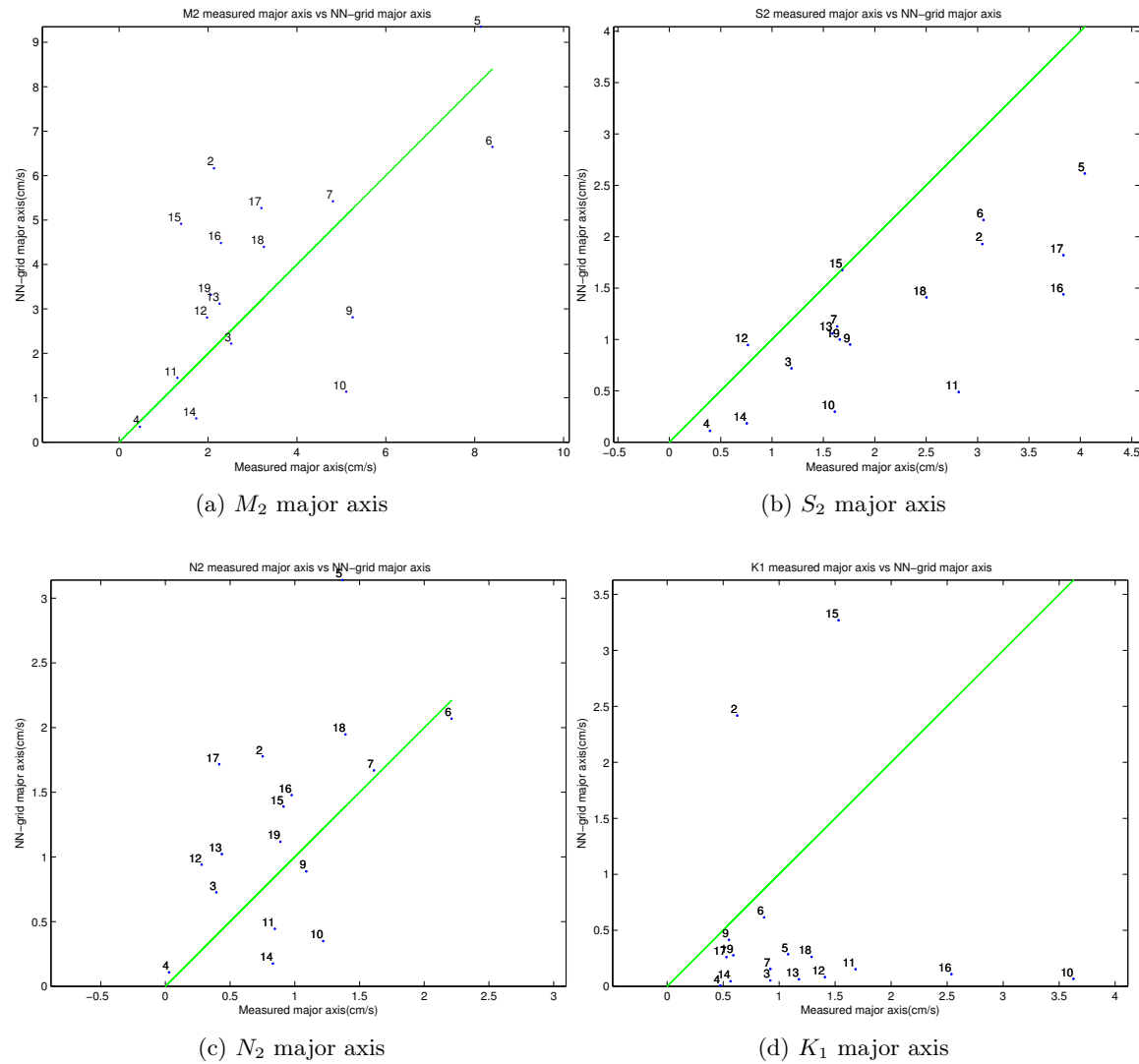(b) S_2 major axis

(c) N_2 major axis

(d) K_1 major axis

Figure 5.14: Major axis between the NN-grid and observations compared

that the model using the coarse NN-grid is estimating the velocities to be slightly higher than what is observed for M_2 and N_2, while the modeled results are on average below the observed values for S_2 and K_1.

To get an overall picture on how the ellipse orientations are thoughout the dataset, the ellipse

orientation angles are compared in Figure 5.15. The two models do not differ much from each other, and they are mostly within $\pm 30°$ which is good considering the circumstances with the locations the validation data comes from.

(a) M_2 ellipse orientation for the Troms-grid

(b) M_2 ellipse orientation for the NN-grid
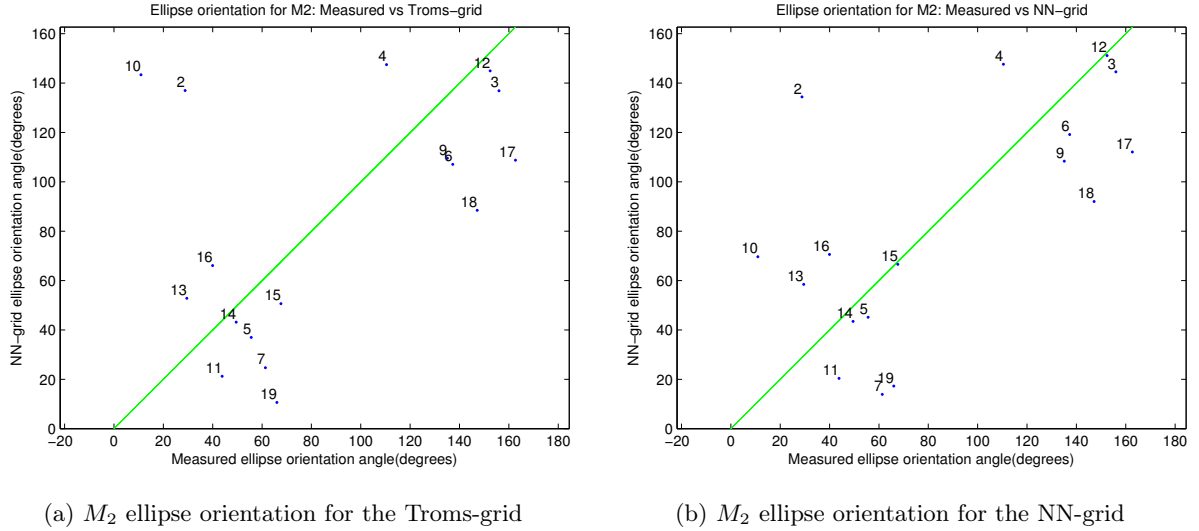
Figure 5.15: M_2 ellipse orientation angle for the both grids

To see if the model using the finer Troms-grid does a more accurate job, Figure 5.16 represents the major axis from the Troms-grid. If compared to Figure 5.14 it is quite clear that the Troms-grid performs even better than the NN-grid. As with the NN-grid, the Troms-grid also has on average M_2 and N_2 slightly above the measured value, and S_2 and K_1 below the measured value. Location 2 is quite off for both M_2 and N_2, and this location is far south-west in the grid close to the boundary, which might explain the error in the modeled results for this location. Locations 5 and 10 is also often among the points which is furthest from the green line which indicates the "perfect match" line. Common for these locations is that they are located quite far north east, and the Troms-grid has low resolution is this area as well, as seen on Figure 4.5

Overall the results from the model when using the Troms-grid manages to produce results closest to the observed values, which was expected. The model using the coarser grid did perform really good as well, and considering how much more work it is to make a grid where many places the resolution is 20-30 meters, vs a grid mostly using 450-500m resolution, it might not be worth all the extra time to obtain the slightly better results. In the end it will depend on the accuracy needed for the application of the model data.
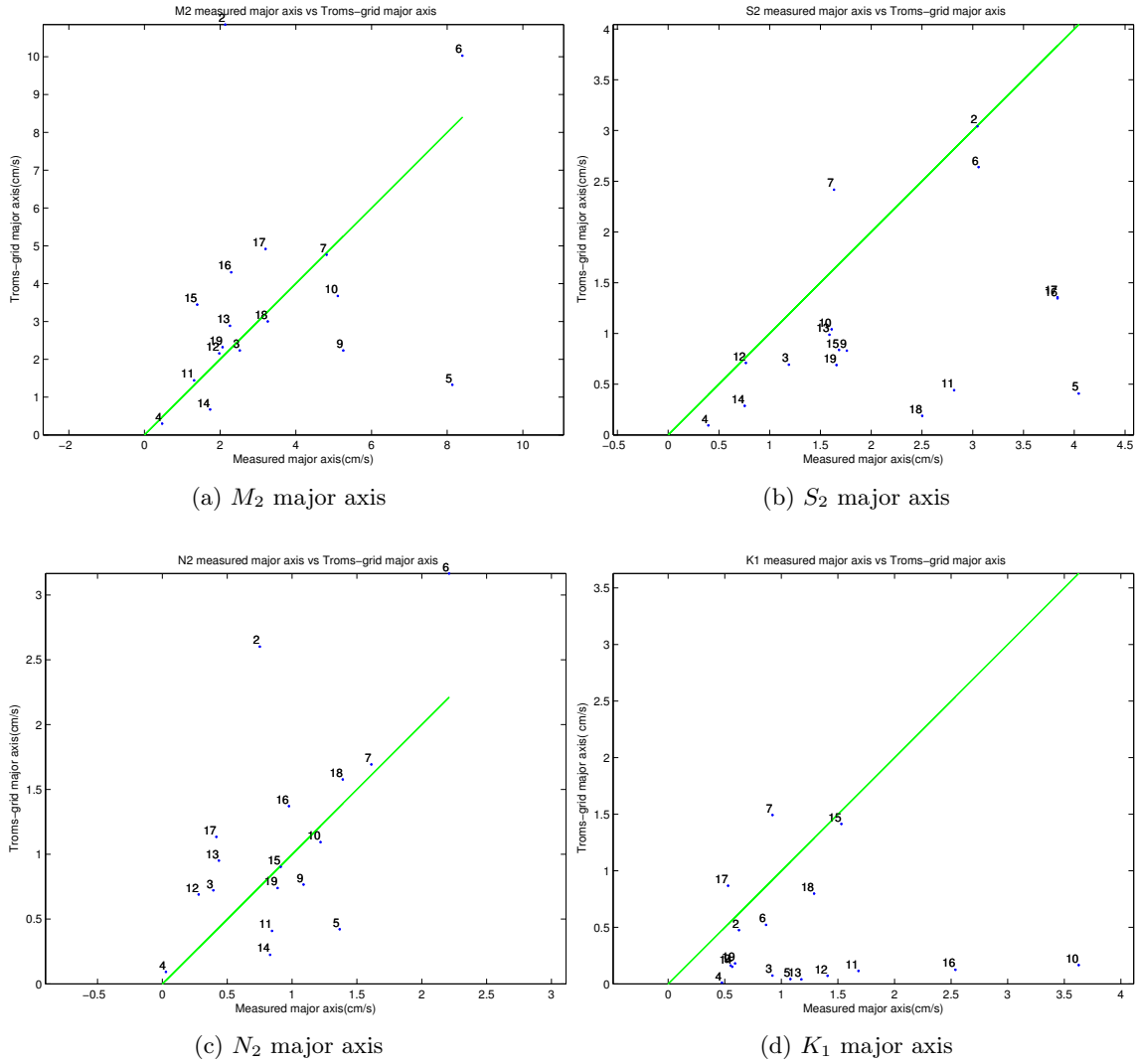
(a) M_2 major axis

(b) S_2 major axis

(c) N_2 major axis

(d) K_1 major axis

Figure 5.16: Major axis between the Troms-grid and observations compared

For the final comparison between the two grids the error of the M_2 major axis and the ellipse orientation angle have been plotted with respect to the model resolution of the given location in Figure 5.17. For the major axis plot, at location 2 an increase in resolution is having a negative effect, while for location 15 the opposite is the case. For locations 5 and 10, the resolution is most coarse compared to the other locations, but the error is not significantly higher here than the average error, so the resolution does not seem to have a significant influence. For the ellipse orientation angles on Figure 5.18, a similar conclusion can be drawn. It should be sufficient to look at M_2, as they other constituents tend to have the same ellipse orientation angle, and close to the same error for the major axis.
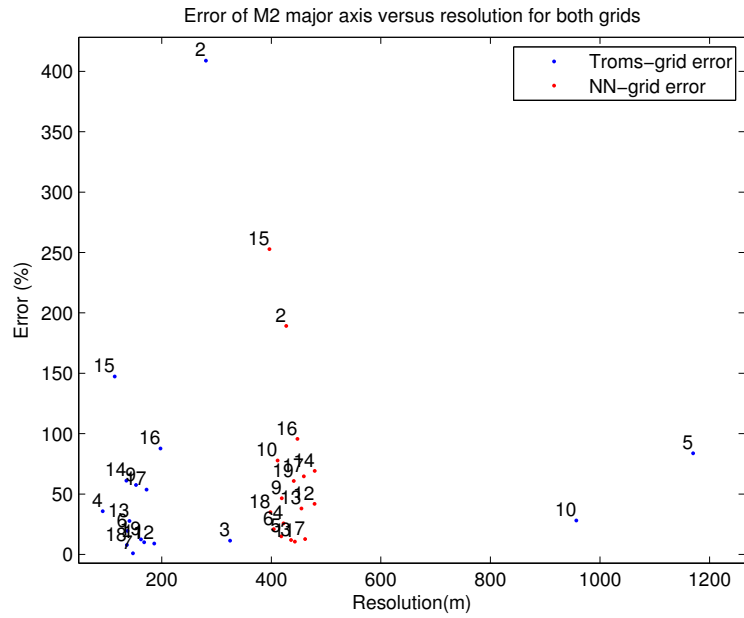
Figure 5.17: M_2 major axis error with resolution along x-axis.
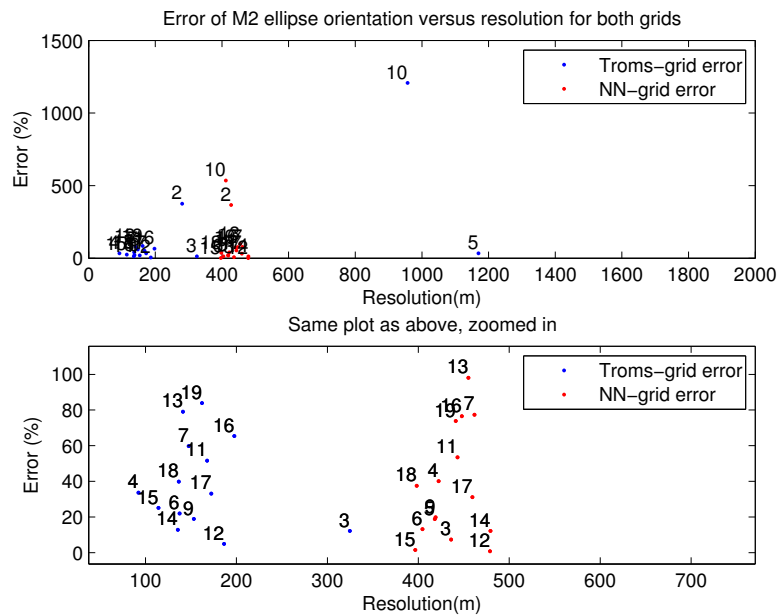
Figure 5.18: M_2 ellipse orientation error with resolution along x-axis.

46

5.0.2 The velocity data set

The locations studied so far have both pressure and velocity measurements. The following datasets lack pressure measurement and spans out of the Troms-grid domain, so the data will only be compared with the NN-grid.

Dataset A

Dataset A has locations A1-A25, and the data is obtained using a SeaGuard RCM instrument, and for most of the locations, the velocity data is measured at 5m, 15m ,3mab (meter above bottom) and at the half depth. In the following figures, four of the locations are displayed with the modeled and measured tidal ellipses.

(a) M_2 at location A3

(b) S_2 at location A3

(c) N_2 at location A3
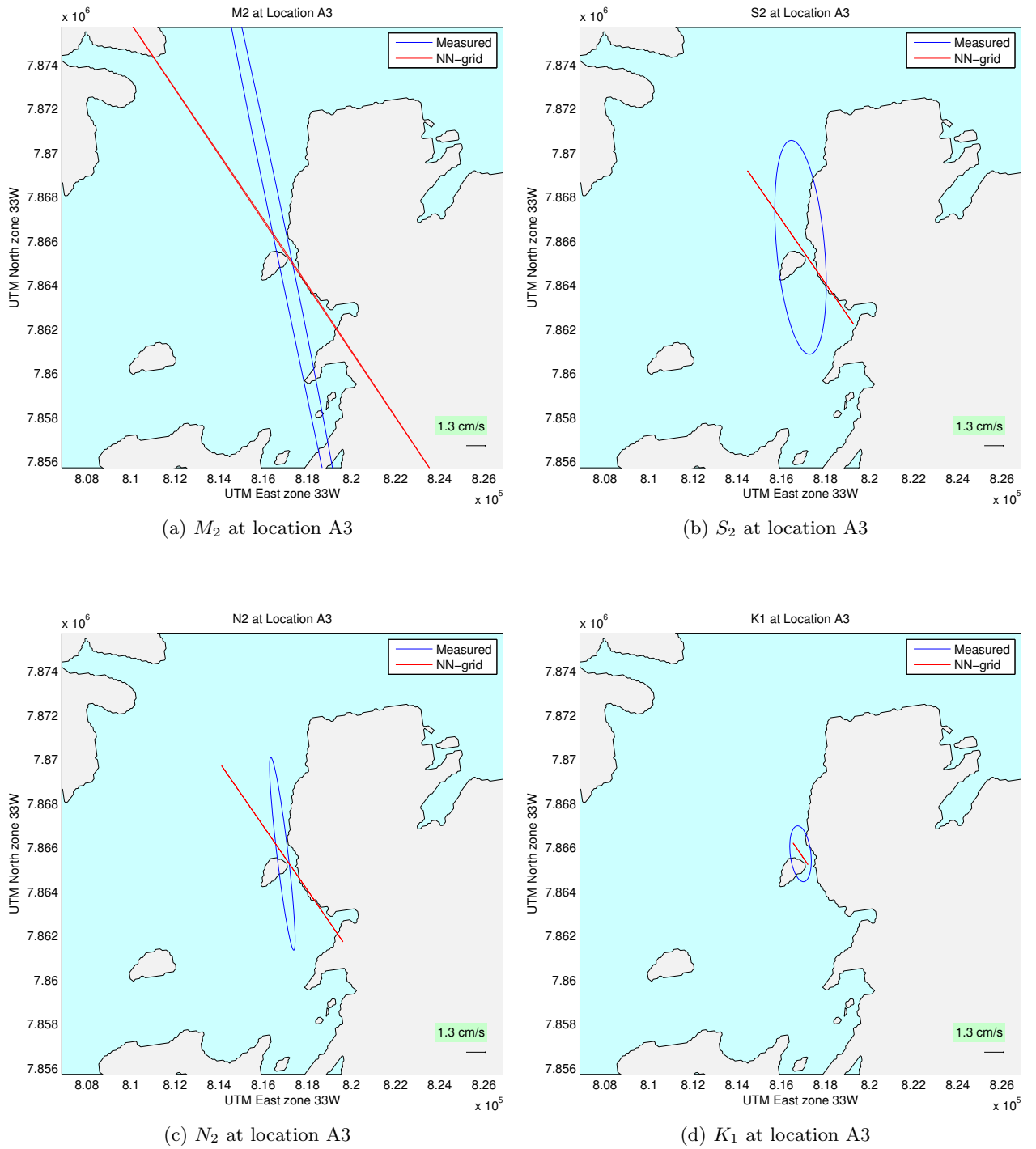
(d) K_1 at location A3

Figure 5.19: Tidal ellipses at location A3

48

(a) M_2 at location A6

(b) S_2 at location A6

(c) N_2 at location A6
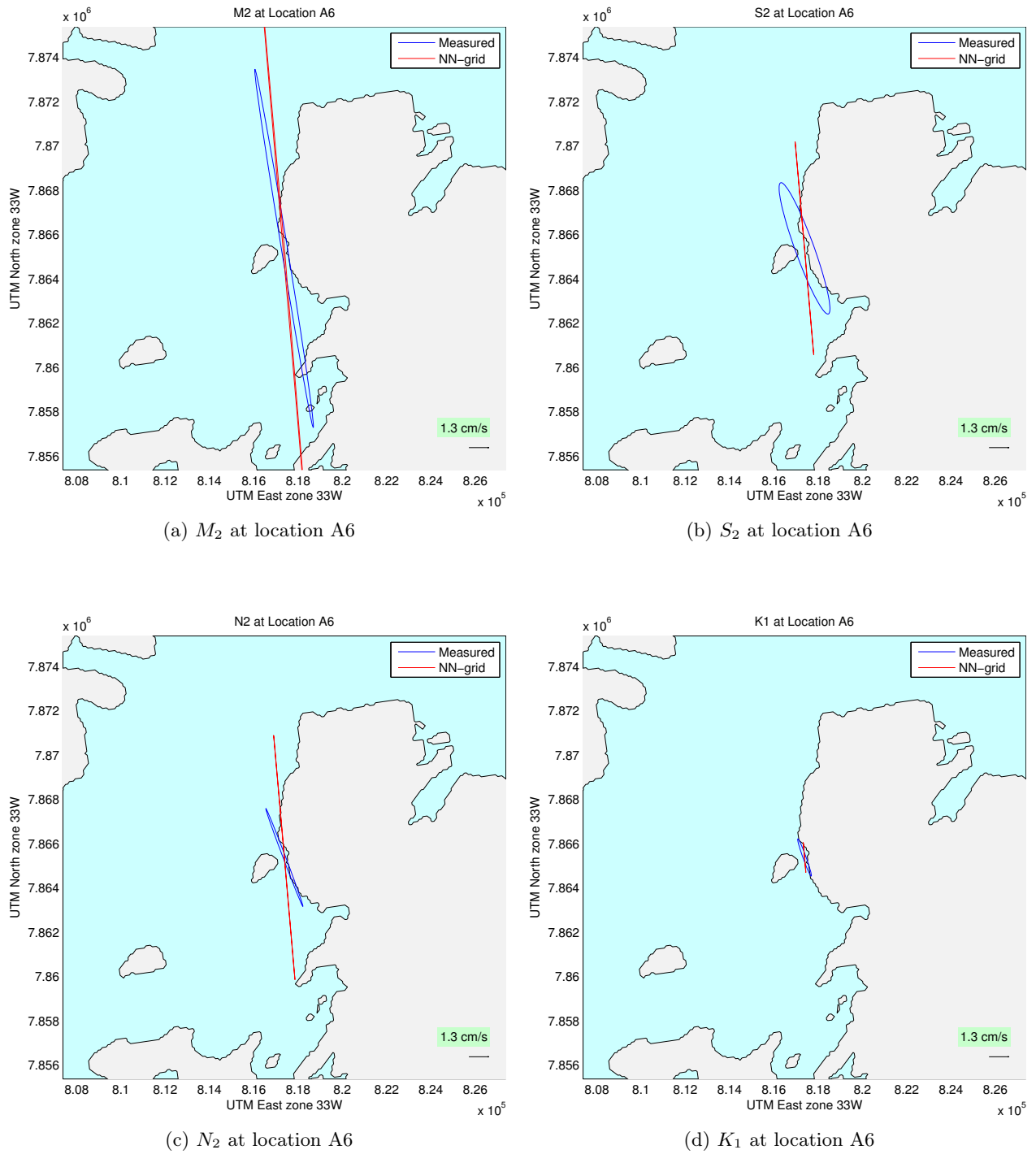
(d) K_1 at location A6

Figure 5.20: Tidal ellipses at location A6

(a) M_2 at location A7

(b) S_2 at location A7

(c) N_2 at location A7
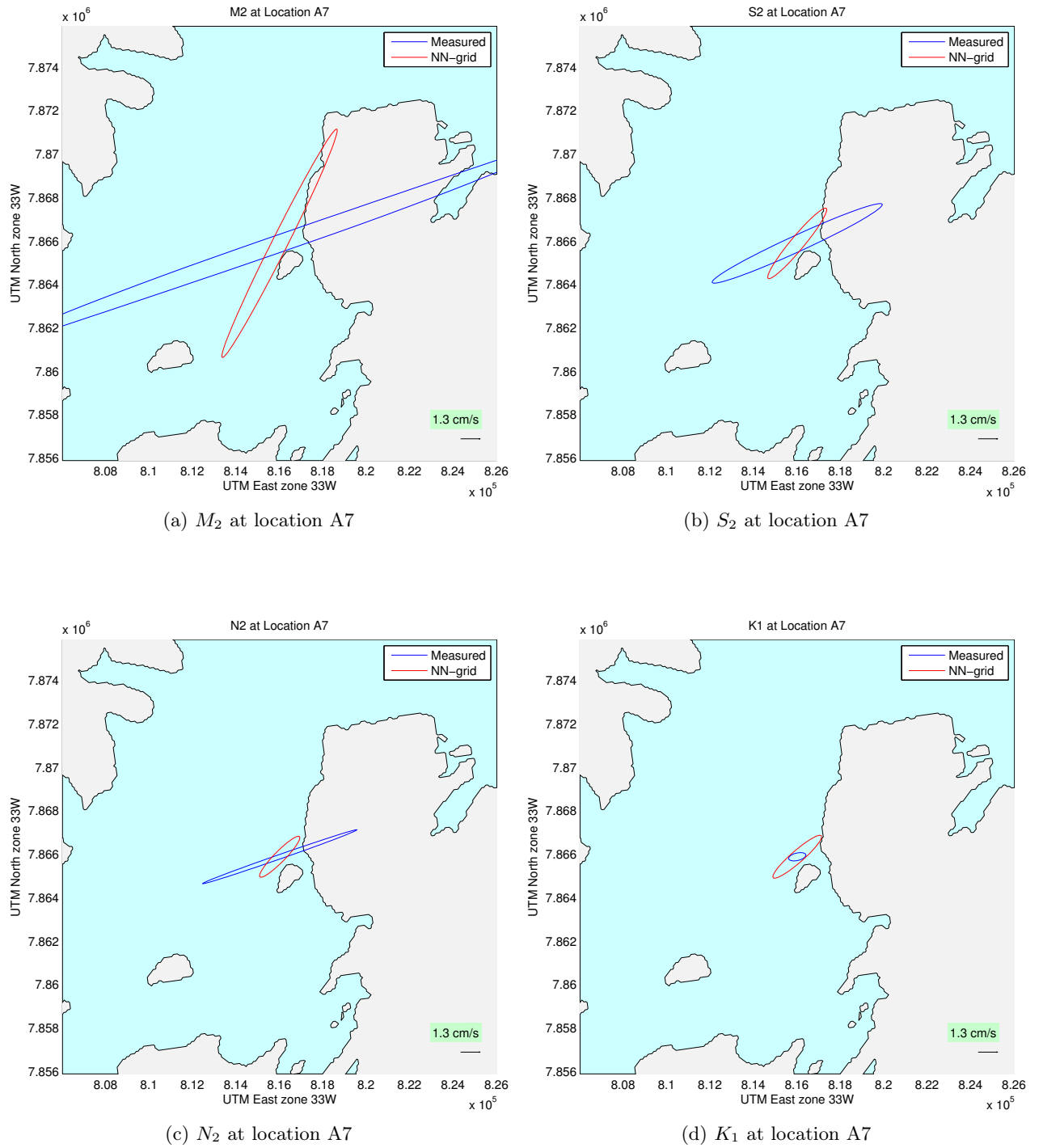
(d) K_1 at location A7

Figure 5.21: Tidal ellipses at location A7

(a) M_2 at location A25

(b) S_2 at location A25

(c) N_2 at location A25
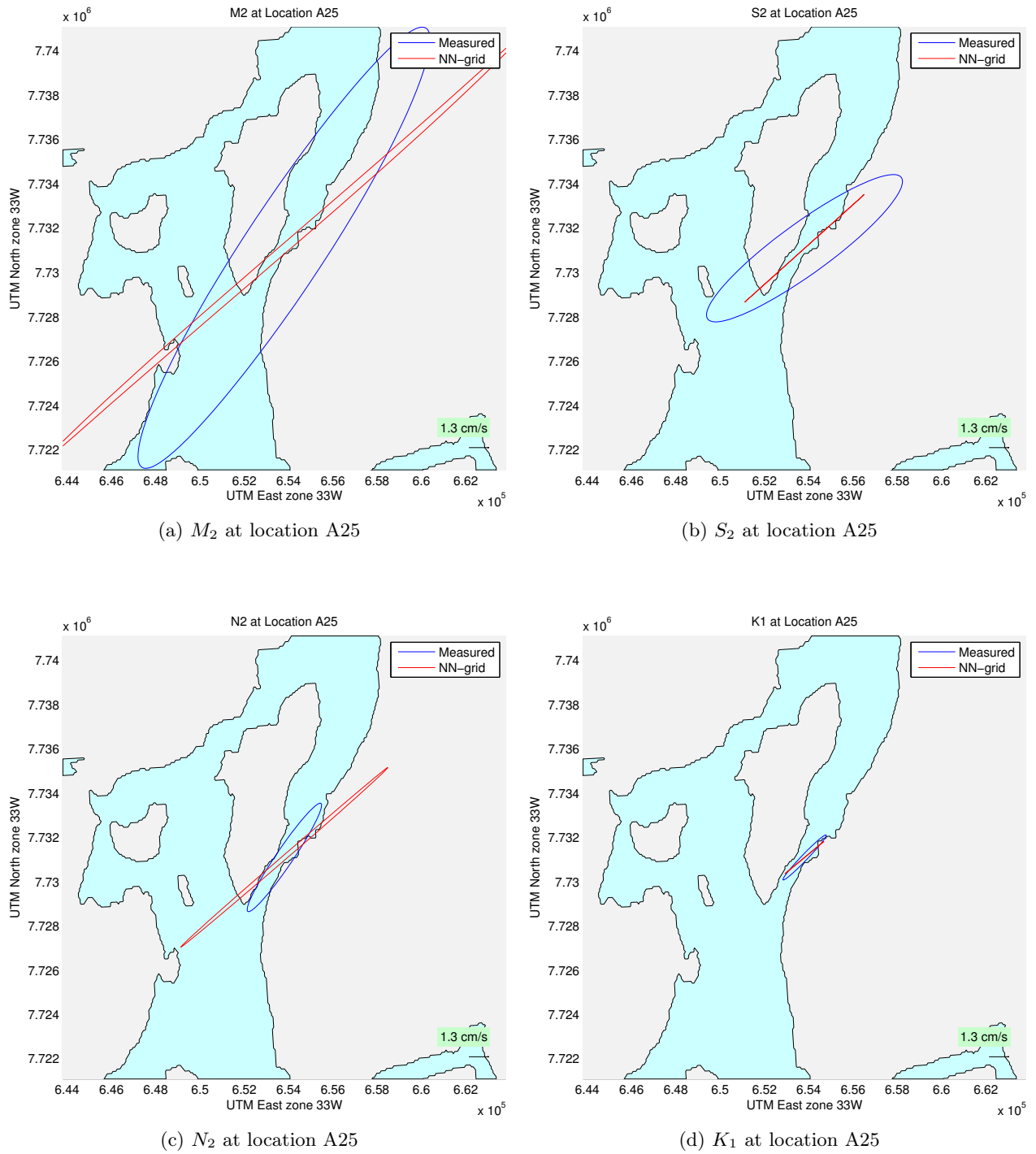
(d) K_1 at location A25

Figure 5.22: Tidal ellipses at location A25

The locations A3, A6 and A7 are quite interesting to compare as they are all close to each other, and involves strong currents. For location A6 the model does a good job at modeling the effects both for M_2 and K_1, while it does a decent job for S_2 and N_2. For location A3 the model is slightly less precise, but it still provides decent results. At location A7 the current is almost perpendicular to the coastline, while the modeled current is less so, and is more in the direction one would guess beforehand. The modeled current is also at lower velocities for M_2, S_2 and N_2, while for K_1 it is to high, so overall the model struggles for this exact location.

The next location A25 just south of Tromsø also involves currents at higher speed, and here ellipse from the modeled data provides a good match with the ellipse from the measured data. It is actually best for K_1 in this scenario, which up until now often has been the constituent the model has struggled most with.

To take a look at all datapoints for A locations, the major axis for M_2, S_2, N_2 and K_1 is plotted in Figure 5.24. Most of the locations in this dataset where in areas where the currents where minimal, hence the grouping of points close to (0,0). The error of the modeled major axis after removing the two most extreme errors, is at 56.3%. A reason for why the error is so high might be that when close to the coastline, which most of the locations are, the measurement depends highly on how close to the shore the measurement is done. As the point in the model closest to the actual location where the measurements was performed can be up to 500 meters away because of the resolution, some errors are bound to be found. This is because the velocity 20 meters from the shore and 500 meters from the shore is likely to differ. In Figure 5.23 the locations are marked on the model domain.
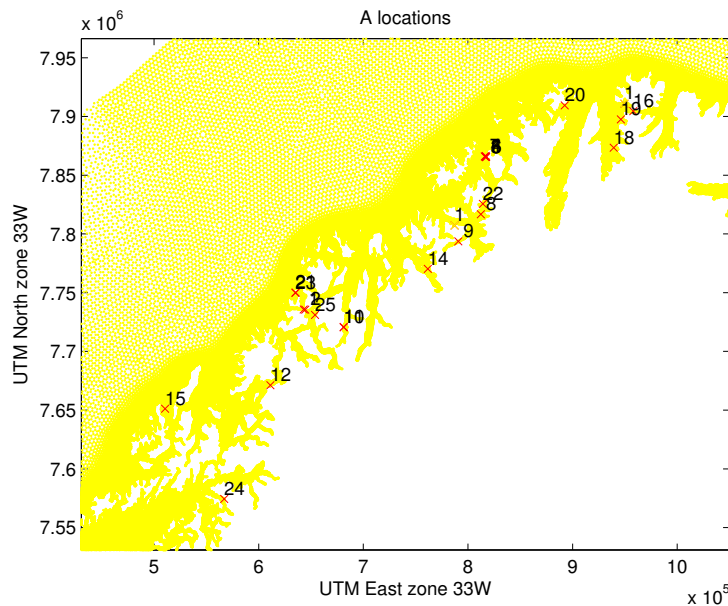

Figure 5.23: Locations for dataset A

(a) M_2 major axis

(b) S_2 major axis

(c) N_2 major axis
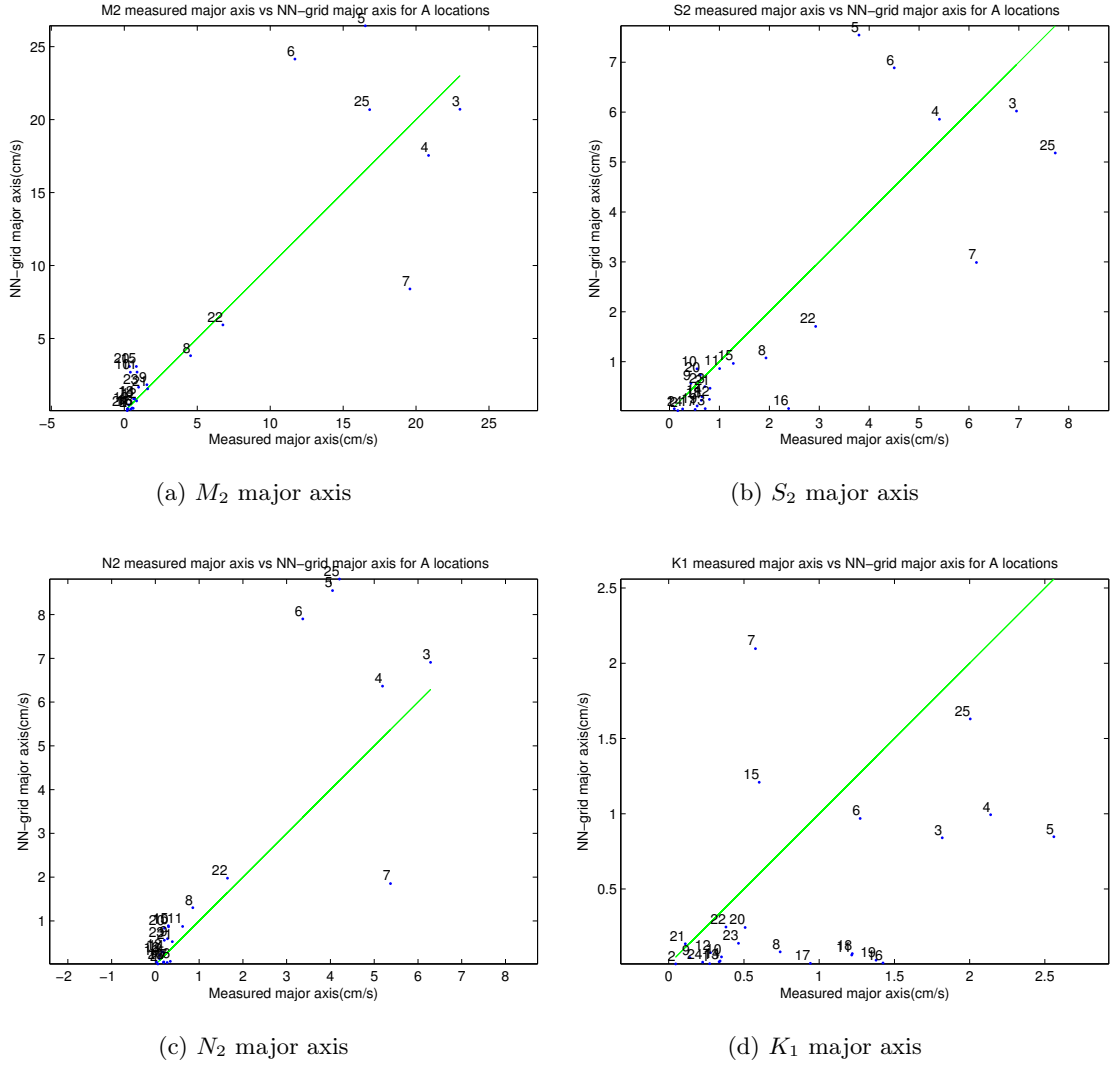
(d) K_1 major axis

Figure 5.24: Major axis between the NN-grid and observations compared

To see how the modeled ellipse orientation correlate with the measured for the entire dataset A, the parameter is plotted in Figure 5.25. The ellipses are quite widely distributed, with only few points close to the green line, which ideally all points should be on. This indicates that the model struggles with the ellipse orientation for most of the locations. Again the fact that the resolution is 500 meters and the validation data comes from locations often close to the shore, the results are not surprisingly bad.
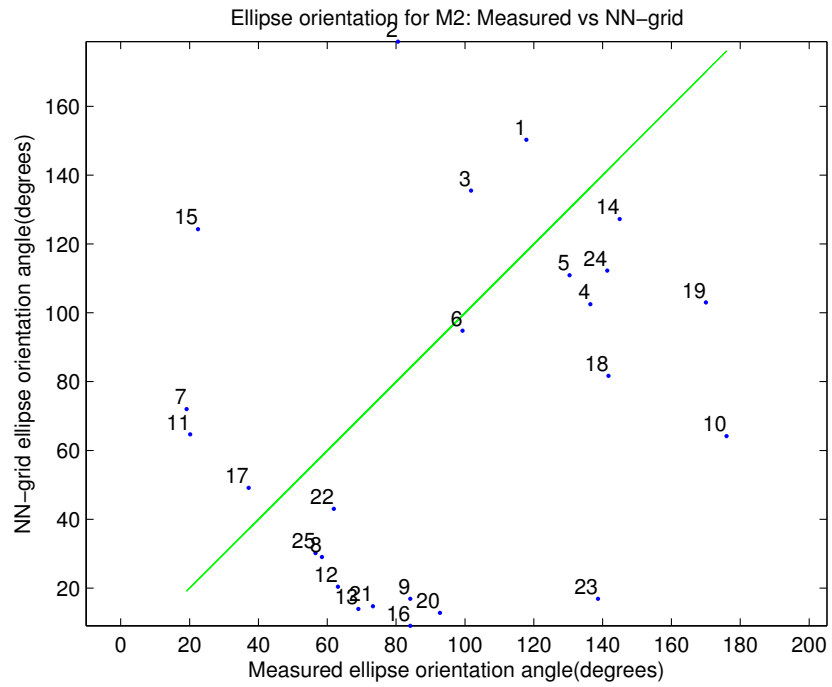
Figure 5.25: Ellipse orientation angle for dataset A for M_2

Dataset B

The next part of the dataset is denoted with location 1B to 35B, and two ellipse plots can be seen below in Figure 5.28 and 5.29. The data in for this location is also obtained using a SeaGuard RCM instrument, and as with dataset A, most of the locations have velocity measurements at 5m, 15m ,3mab (meter above bottom) and at the half depth.

Location 16 on Figure 5.28 shows a more or less perfect agreement for a low velocity location between modeled and measured results for all constituents but K_1, which is the constituent the model overall seems to be struggling the most with.

The other location, seen on Figure 5.29 shows an example of measurement data and model data almost perpendicular to each other. The amplitude of the velocity is good for M_2 and N_2, but the direction is quite far off for all four constituents.

To see how the ellipse orientation match for the 35 locations the ellipse orentation angle can be seen in Figure 5.26. As with location A, the points are quite widely spread, so again the model struggles.
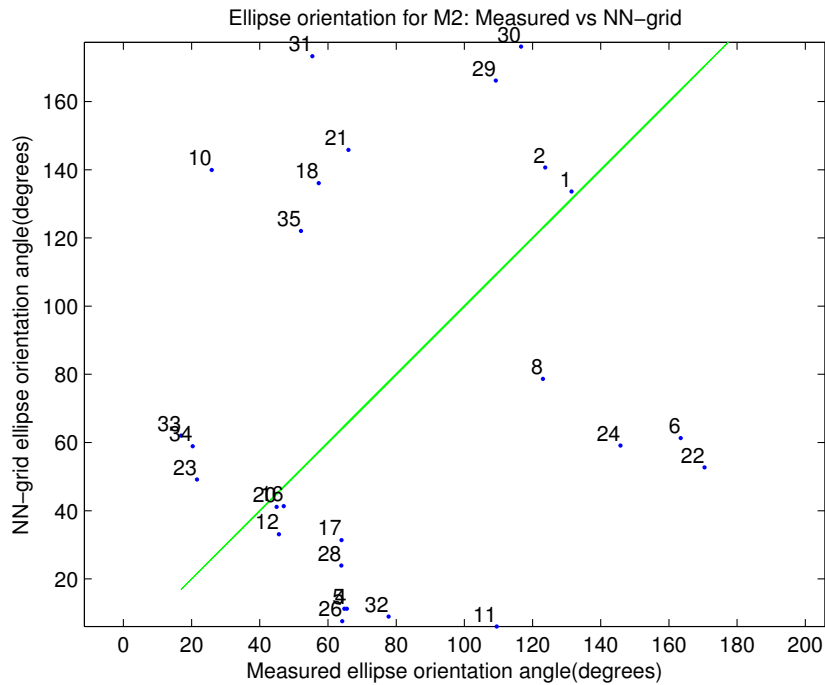

Figure 5.26: M_2 ellipse orientation for B locations

To get an overview of the amplitude of the velocity for the 35 location, their major axis are plotted, modeled versus measured, on Figure 5.27. Again the model results in M_2 and N_2 slightly higher than the measured, while S_2 and K_1 is on average lower than the values measured.

(a) M_2 major axis
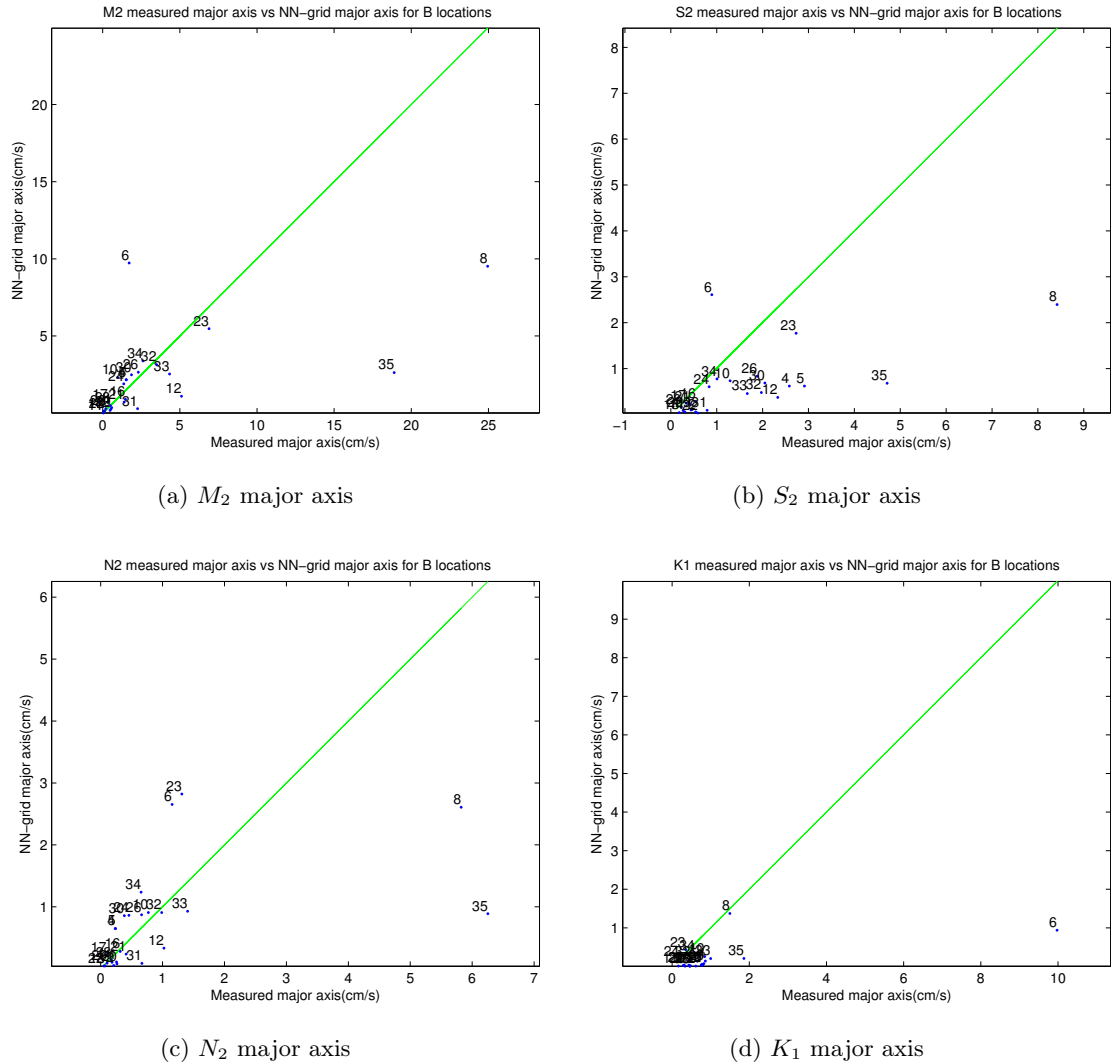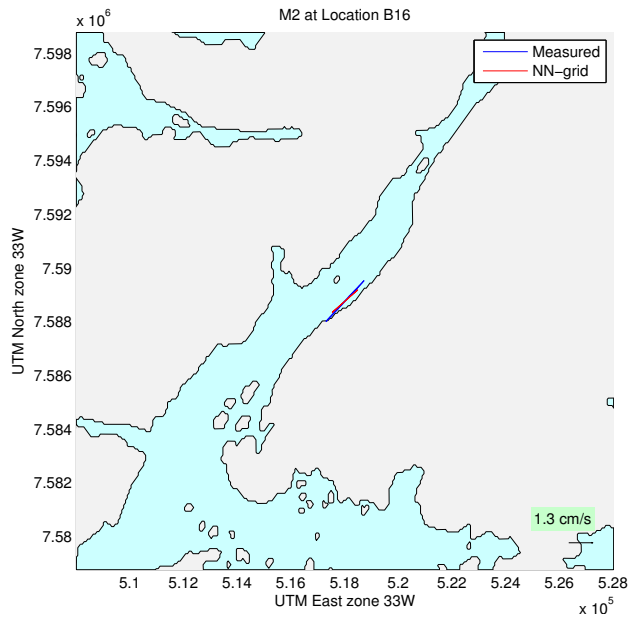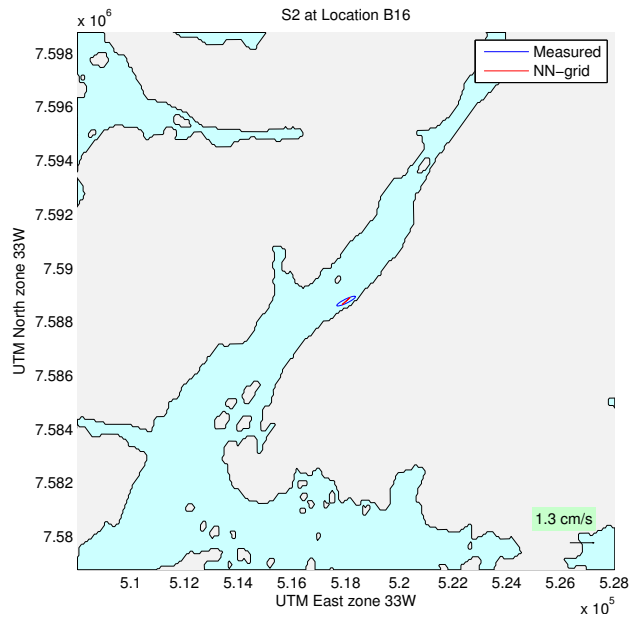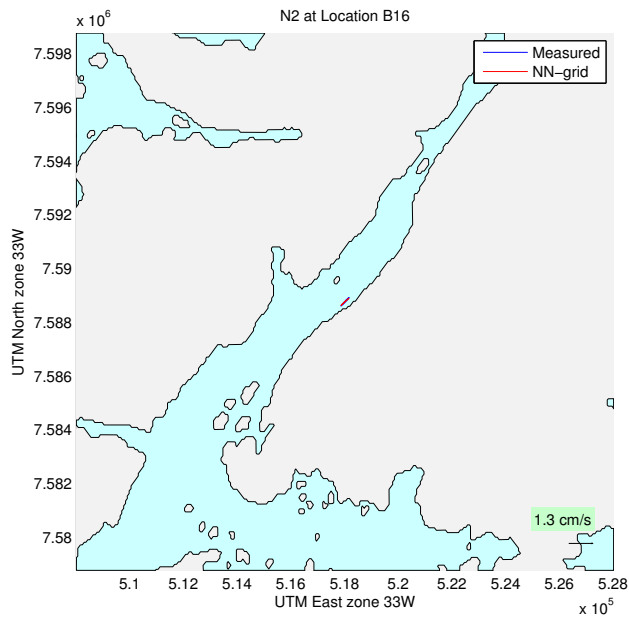
(b) S_2 major axis

(c) N_2 major axis

(d) K_1 major axis

Figure 5.27: Major axis between the Troms-grid and observations compared

56
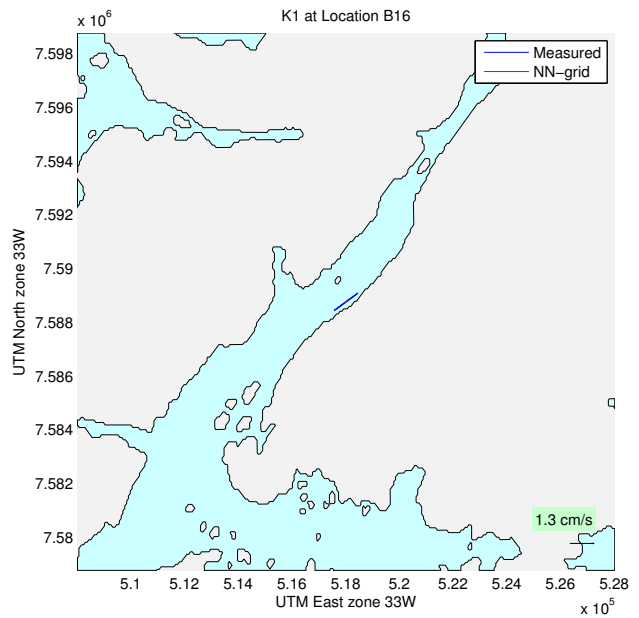
(a) M_2 at location B16

(b) S_2 at location B16

(c) N_2 at location B16

(d) K_1 at location B16

Figure 5.28: Tidal ellipses at location B16

(a) M_2 at location B26

(b) S_2 at location B26

(c) N_2 at location B26
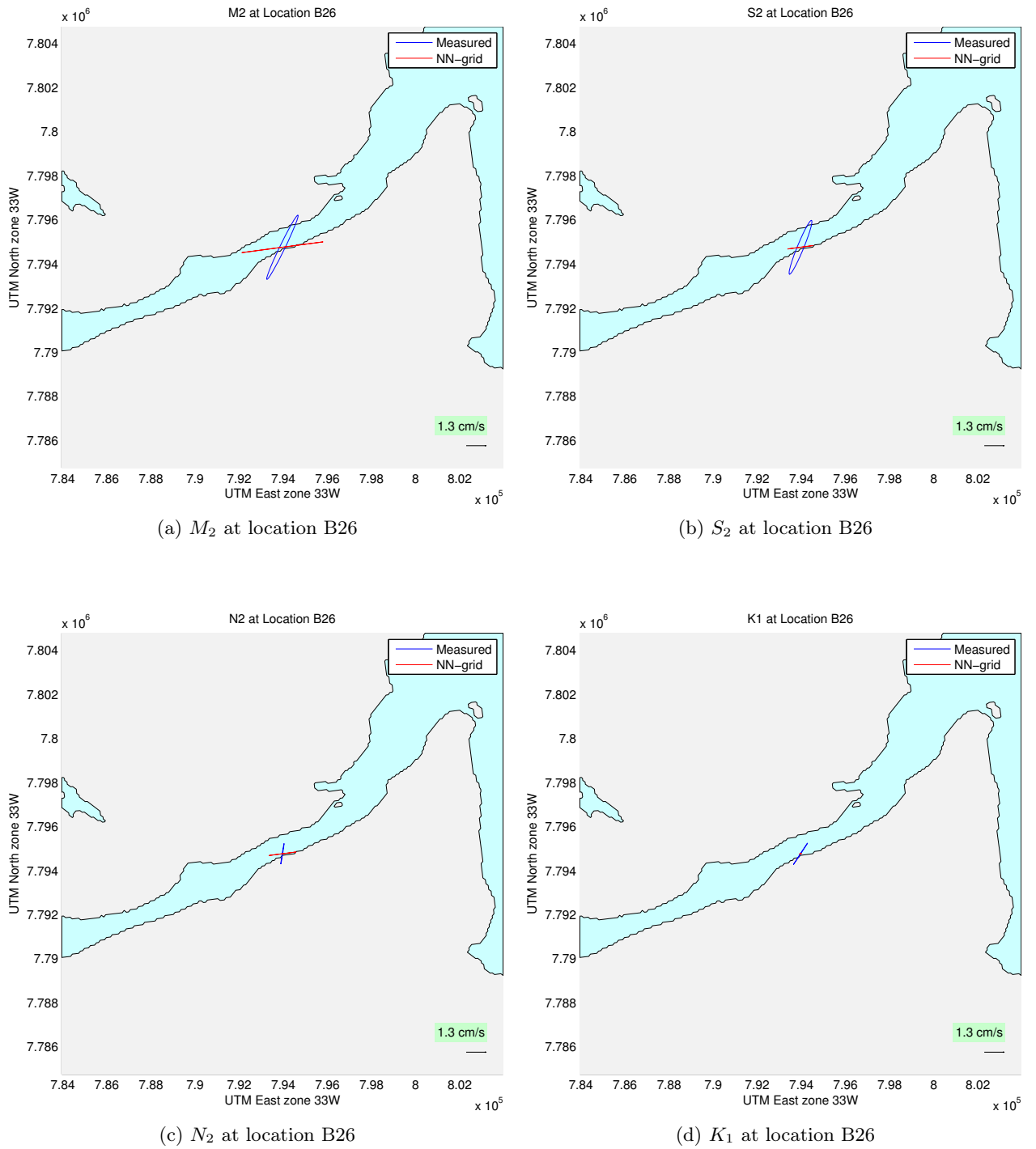

(d) K_1 at location B26

Figure 5.29: Tidal ellipses at location B26

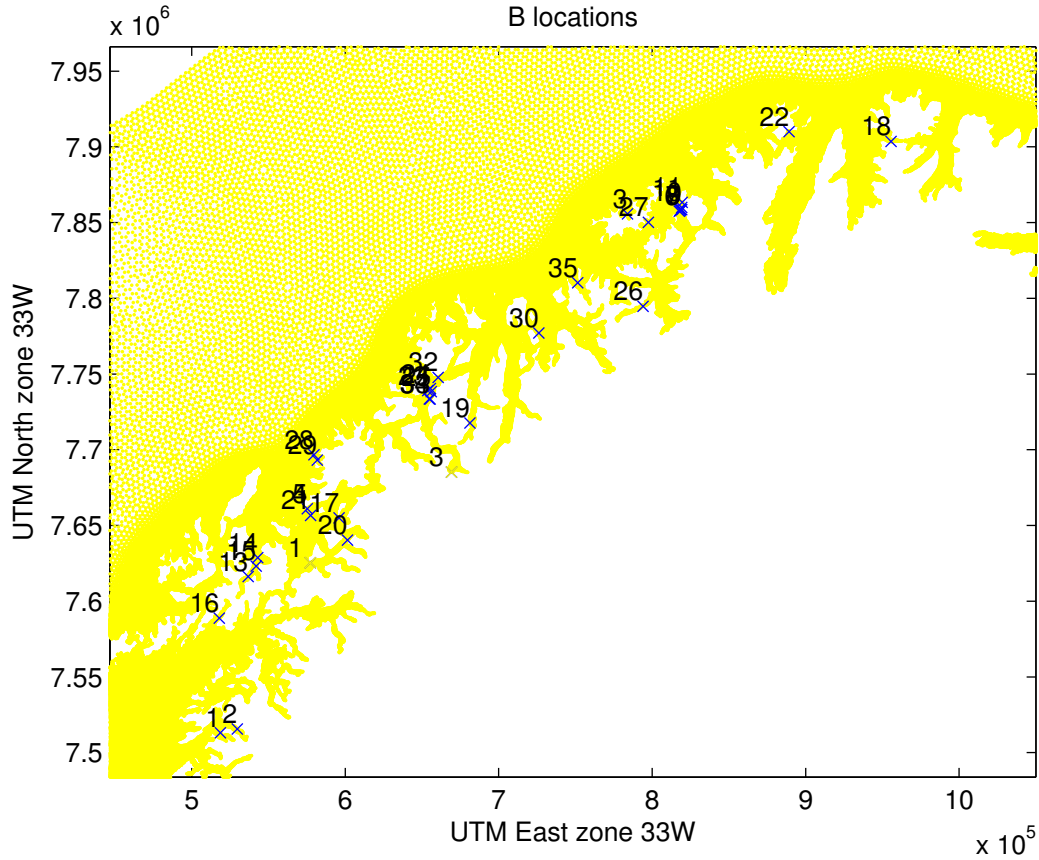Figure 5.30 shows where the locations are located within the grid modeled.

Figure 5.30: Dataset B locations

C locations

The last dataset consists of data obtained using rotor instrument. They have lower accuracy than the seaguard instruments, but Akvaplan-Niva has a big amount of data obtained using this instrument, and for the purpose of validating a model, they should be more than accurate enough.
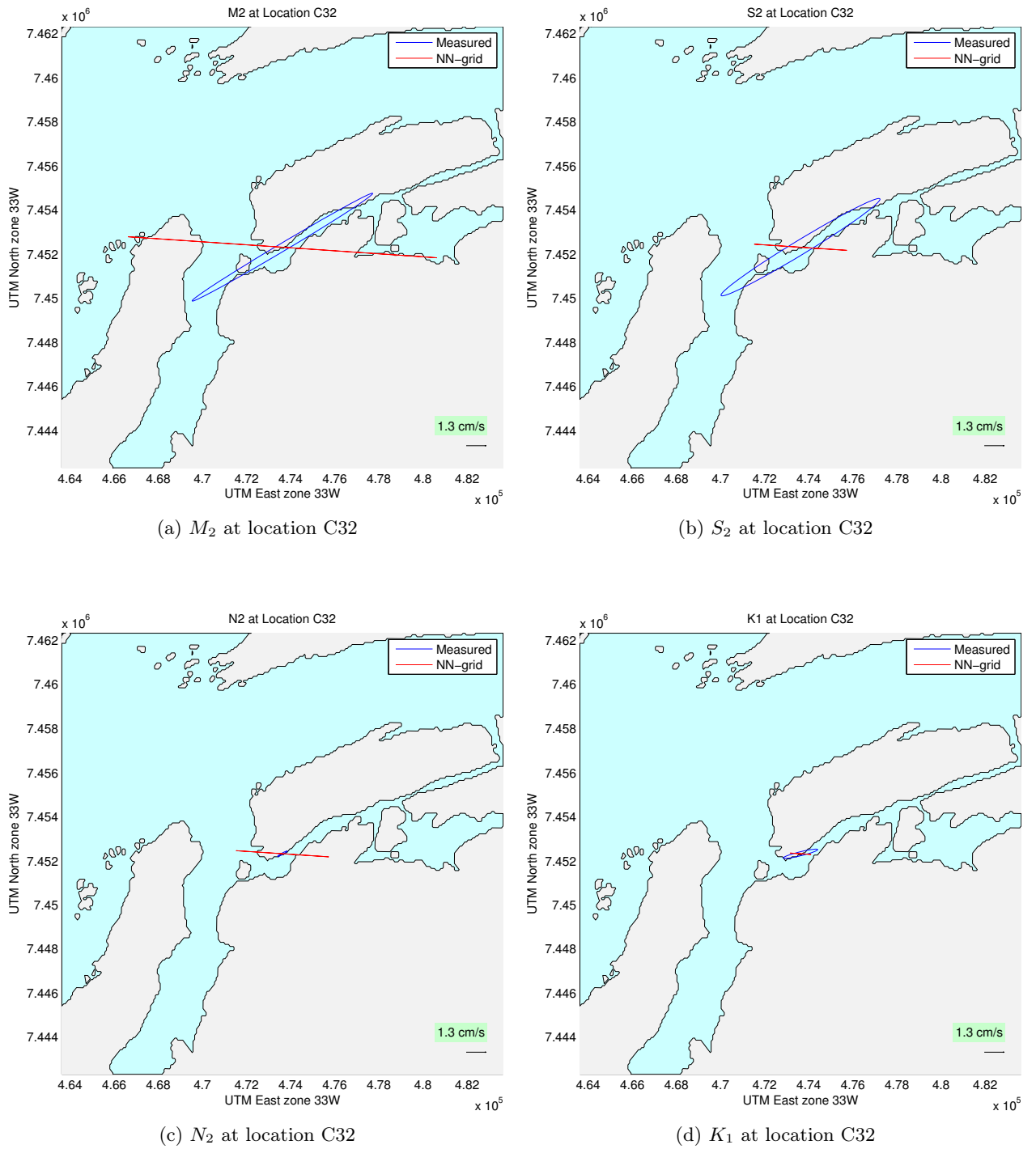
(a) M_2 at location C32

(b) S_2 at location C32

(c) N_2 at location C32

(d) K_1 at location C32

Figure 5.31: Tidal ellipses at location C32

60

(a) M_2 at location C35

(b) S_2 at location C35

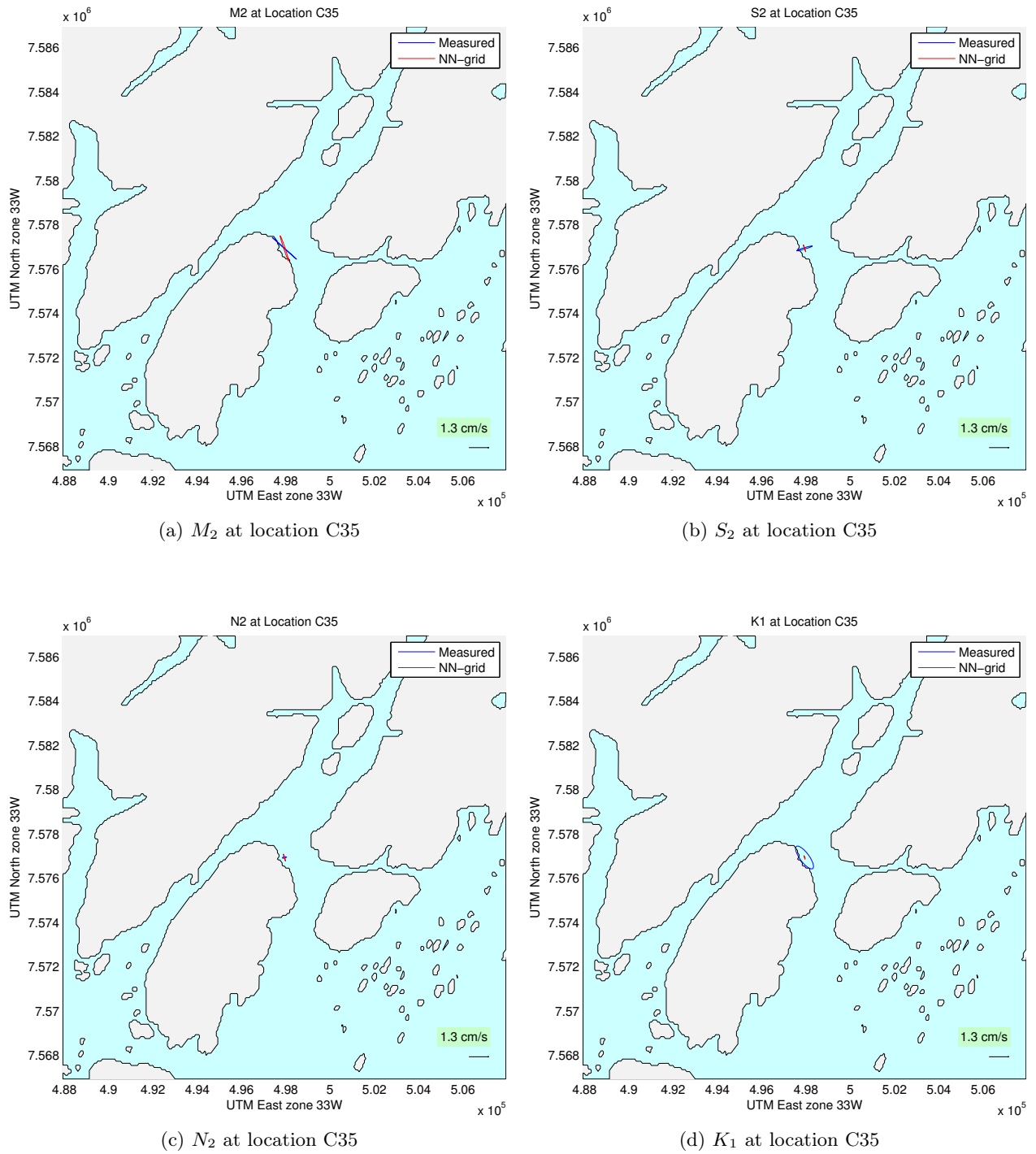(c) N_2 at location C35

(d) K_1 at location C35

Figure 5.32: Tidal ellipses at location C35

For location C32 it can be seen on Figure 5.31 that the magnitude of the velocity is good for M_2 and K_1, while the direction is off by quite a bit. Here the measured ellipse provide the direction which seems intuitively most accurate as it is directed along the shore, while the modeled ellipse is headed more towards the shore.

The last location illustrated with ellipses is C35 on Figure 5.32. This location is in an area with complex geometry and still the results from the model is quite good. Again K_1 is the constituent which deviates the most from the validation ellipse.

To get an overall impression for the C locations, consider Figure 5.33 for the ellipse major axis and Figure 5.34 for the ellipse orientation angles. Figure 5.33 is much like the corresponding for location A and B, with a wide spread of angles, indicating that the model seem to struggle with the current directions. For the major axis on Figure 5.34 the model is again overestimating the major axis for M_2 and N_2, while underestimating S_2 and K_1.
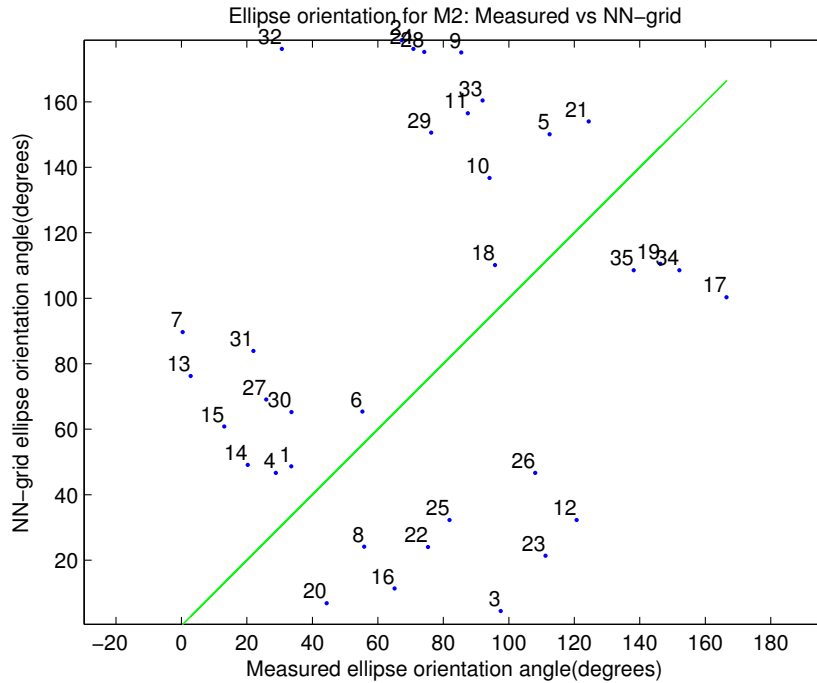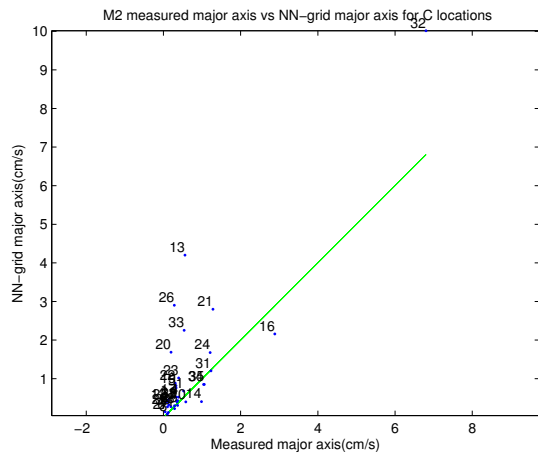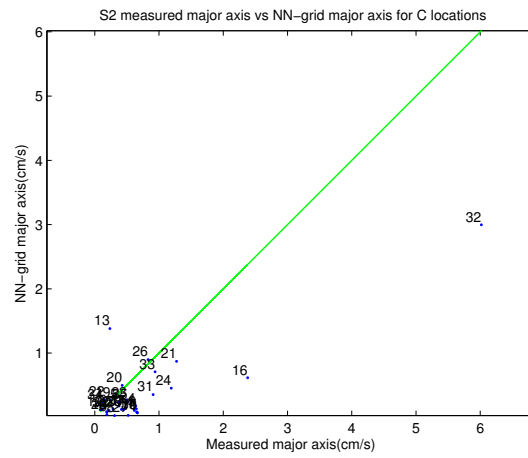

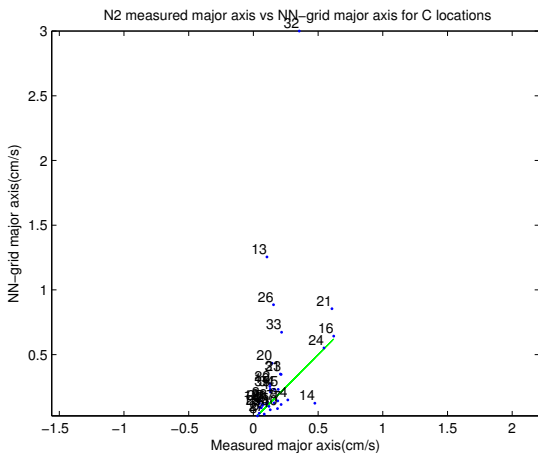Figure 5.33: M_2 ellipse orientation for C locations

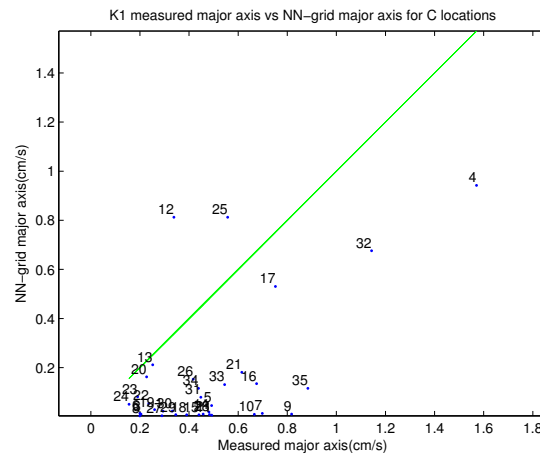For a map over all the C-locations, see Figure 5.35

(a) M_2 major axis

(b) S_2 major axis

(c) N_2 major axis

(d) K_1 major axis

Figure 5.34: Major axis between the NN-grid and observations compared for location C
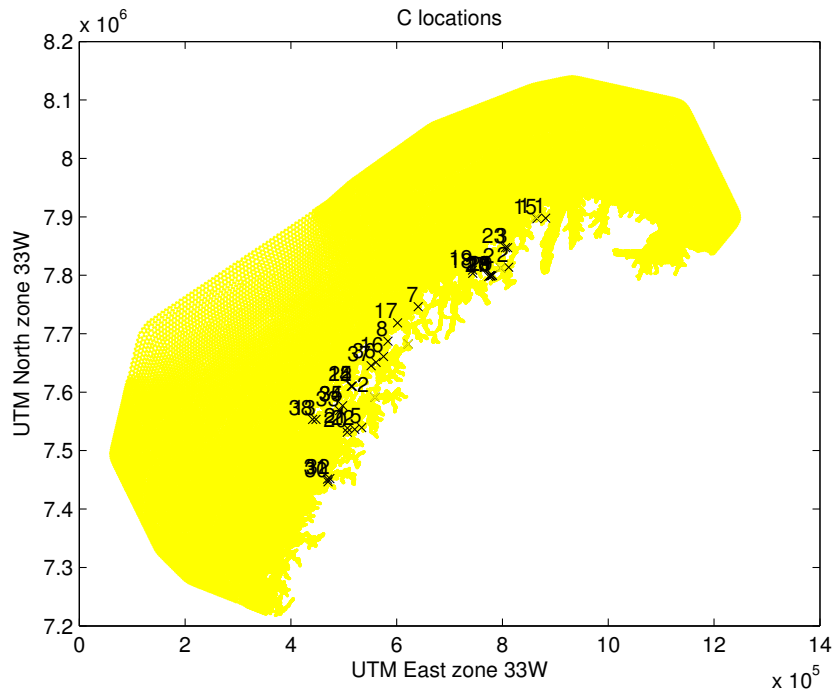
Figure 5.35: Locations of dataset C

Chapter 6

Conclusion

The model FVCOM has been verified against a large number of measurements, both for tidal elevations and tidal currents. The focus has been on verifying the model in a two-dimesional setup with depth integrated equations. Two different grids have been employed to see the effect of a fine vs coarse grid. Matlab has been used to analyze the tidal data and to extract the tidal constituents of interest.

From the dataset with pressure measurements, the tidal constituents M_2, S_2, K_1 and O_1 where studied in detail to see how the different constituent contributes to the final tide observed. M_2 proved to be the main contributer of the four, followed by S_2, while K_1 and O_1 was close to insignificant in comparison. Overall, the coarser grid covering the entire Northern Norway had a mean error of 4.35% for M_2 and 25.54% error for S_2, while the Troms-grid, with a much higher resolution ended up with a mean error of 5.04% for M_2 and 27.11%. This was not expected, as one would expect more precise results when using a more precise grid. The most probable reason behind this odd result is the way the boundary for the Troms-grid is defined at the southern boundary. The boundary goes straight through Lofoten islands which has been shown to alter the tidal wave propagating northwards by a large factor. This effect, which can be seen in Figure 1.1, is believed to be the cause of the lack of performance for the Troms-grid together with the fact that the resolution in Vestfjorden where the tidal waves enters the domain is much lower for this grid than for the NN-grid. This means that the damage is already done, and as the wave propagates northwards along the coast, so does the error induced by the not so ideal southern boundary location.

For the velocity analysis of the dataset, the two grids is mostly in good agreement with each other, and the model results often matches the verification-data. The difference between the two grids when it comes to ellipse orientation angle is minimal, but considering the major axis, the Troms-grid does a slightly better job, resulting in an overall better performance over the NN-grid. However, this is minimal, and if it is worth the model run time of almost 12 hours versus the NN-grid which only uses around 4 hours when modeled can be questioned. It is interesting that the tidal ellipses matches overall pretty good, considering the modeled velocities are averaged over the entire depth, while the verification data only recorded the velocity at the bottom. Also many of the locations the verification data are recorded are at unfavorable places, not representing the general tidal currents in the surrounding area. Also, the initial dataset included in total almost 150 separate locations, but only around 110 ended up beeing used. Several of the excluded points

had a record length which was to short to perform proper analysis with, while some had wrong coordinates. It is highly probable that not all the locations with errors in coordinates are removed, as only locations which are clearly out of place are detectable. The issue with local topography is also making the process of verification hard. Hence it is hard to identify the reason for why at certain locations the measured and modeled results deviates greatly from one another.

For dataset A, B and C, most of the locations consists of velocity averages over 5m depth, 15m depth, bottom and in the middle of the water column, and only the NN-grid is being compared to the measured data. In general, the tidal constituents M_2 and N_2 tend to be modeled at too high velocity, while S_2 and K_1 tend to be at a too low velocity relative to the verification data. This indicates that the boundary input might involve minor errors, and by slightly reducing M_2 and N_2 at the boundary, while increasing S_2 and K_1 might reduce the overall error. Unfortunately most of the locations had velocities ranging from 0-2 cm/s, resulting in a verification dataset not ideal for testing the models performance at a variety of current speeds. For the high speed locations present, the model did not seem to struggle more than with the low speed locations. Also, the model performed just as well close to the open sea as it did inside deep fjords and in areas with complex geometries. Combining all the major axis errors for dataset A, B and C, and removing the 5% biggest outliers, results in an average error of 83.9% for M_2, 57.0% for S_2, 76.6% for N_2 and 76.9% for K_1.

6.1 Future work

The task of verifying the model can be taken much further, given time. Implementing 3D equations, and thus include salinity and temperature should improve the results. This would also allow for velocities at different model depth to be extracted and compared with the same exact depth from measurements.

It is also possible to extract data from the older measurements done, to increase the validation data set. Another possibility is to study the effect of increasing the resolution of the coarser model along the coast will have on the simulation. The bottom friction could also be increased or decreased, and the boundary input modified.

To compare FVCOM results with results from the model ROMS which uses a structured grid would also be of interest. If ROMS is already validated for certain areas, the model can possibly be used to verify FVCOM results for the same areas ROMS is known to perform well.

Bibliography

[Azerad and Guillen, 2001] Azerad, P. and Guillen, F. (2001). Mathematical justification of the hydrostatic approximation in the primitive equations of geophysical fluid dynamics. SIAM Journal on Mathematical Analysis, 33(4):847–859.

[B, 2001] B, G. (2001). Moskstraumen. myter, dikting og virkelighet. In Arbok, Det Norske Videnskaps-Akademi, page p. 157–69.

[Berntsen, 2002] Berntsen, J. (2002). Internal pressure errors in sigma-coordinate ocean models. Journal of Atmospheric & Oceanic Technology, 19(9).

[Blumberg and Mellor, 1987] Blumberg, A. F. and Mellor, G. L. (1987). A description of a three-dimensional coastal ocean circulation model. Coastal and estuarine sciences, 4:1–16.

[CHEN et al., 2006] CHEN, C., BEARDSLEY, R. C., and COWLES, G. (2006). Finite volume coastal ocean. Oceanography, 19(1):78.

[Chen et al., 2013] Chen, C., Cowles, G., and Beardsley, R. (2013). An unstructured grid, finite-volume coastal ocean model: Fvcom user manual. SMAST/UMASSD.

[Chen et al., 2009] Chen, C., Gao, G., Qi, J., Proshutinsky, A., Beardsley, R. C., Kowalik, Z., Lin, H., and Cowles, G. (2009). A new high-resolution unstructured grid finite volume arctic ocean model (ao-fvcom): An application for tidal studies. Journal of Geophysical Research: Oceans (1978–2012), 114(C8).

[Chen et al., 2003] Chen, C., Liu, H., and Beardsley, R. C. (2003). An unstructured grid, finite-volume, three-dimensional, primitive equations ocean model: application to coastal ocean and estuaries. Journal of atmospheric and oceanic technology, 20(1):159–186.

[Codiga, 2011] Codiga, D. L. (2011). Unified tidal analysis and prediction using the UTide matlab functions. Graduate School of Oceanography, University of Rhode Island.

[Colling et al., 1989] Colling, A., Park, D., Phillips, J., Rothery, D., Wright, J., and Brown, J. (1989). Waves, tides and shallow-water processes. Butterworth-Heinemann.

[Debreu and Blayo, 2008] Debreu, L. and Blayo, E. (2008). Two-way embedding algorithms: a review. Ocean Dynamics, 58(5-6):415–428.

[Dick, 1992] Dick, E. (1992). Introduction to finite volume techniques in computational fluid dynamics. In Computational fluid dynamics, pages 261–288. Springer.

[Eggvin, 1932] Eggvin, J. (1932). Vannlagene på fiskefeltene. Arsberetning Norges Fiskerier, 2:90–95.

[Eggvin, 1934] Eggvin, J. (1934). De oceanografiske forhold i vestfjorden og deres sammenheng med lofotfisket 1933. Arsberetning Norges Fiskerier, 2:94–102.

[Eliassen et al., 2001] Eliassen, I. K., Heggelund, Y., and Haakstad, M. (2001). A numerical study of the circulation in saltfjorden, saltstraumen and skjerstadfjorden. Continental Shelf Research, 21(15):1669–1689.

[Engedahl, 1995] Engedahl, H. (1995). Use of the flow relaxation scheme in a three-dimensional baroclinic ocean model with realistic topography. Tellus A, 47(3):365–382.

[Foreman, 1977] Foreman, M. (1977). Manual of tidal heights analysis and prediction. pacific marine sciences report 77-10. institute of ocean sciences. victoria. British Columbia, 77-10:.

[Foreman and Henry, 1989] Foreman, M. and Henry, R. (1989). The harmonic analysis of tidal model time series. Advances in water resources, 12(3):109–120.

[Fox, 2002] Fox, J. (2002). An R and S-Plus companion to applied regression. Sage.

[Gjevik, 2009] Gjevik, B. (2009). Flo og fjære langs kysten av norge og svalbard.

[Godin, 1973] Godin, G. (1973). The analysis of tides. The analysis of tides., by Godin, G.. Liverpool (UK): Liverpool University Press, 264 p., page 264.

[Grabbe et al., 2009] Grabbe, M., Lalander, E., Lundin, S., and Leijon, M. (2009). A review of the tidal current energy resource in norway. Renewable and Sustainable Energy Reviews, 13(8):1898–1909.

[Gray and Giorgini, 1976] Gray, D. D. and Giorgini, A. (1976). The validity of the boussinesq approximation for liquids and gases. International Journal of Heat and Mass Transfer, 19(5):545–551.

[Haidvogel et al., 1991] Haidvogel, D. B., Wilkin, J. L., and Young, R. (1991). A semi-spectral primitive equation ocean circulation model using vertical sigma and orthogonal curvilinear horizontal coordinates. Journal of Computational Physics, 94(1):151–185.

[Huang et al., 2008] Huang, H., Chen, C., Cowles, G. W., Winant, C. D., Beardsley, R. C., Hedstrom, K. S., and Haidvogel, D. B. (2008). Fvcom validation experiments: Comparisons with roms for three idealized barotropic test problems. Journal of Geophysical Research: Oceans (1978–2012), 113(C7).

[Leffler and Jay, 2009] Leffler, K. E. and Jay, D. A. (2009). Enhancing tidal harmonic analysis: Robust (hybrid l1/l2) solutions. Continental Shelf Research, 29(1):78–88.

[Lynch and Naimie, 1993] Lynch, D. R. and Naimie, C. E. (1993). The m2 tide and its residual on the outer banks of the gulf of maine. Journal of Physical Oceanography, 23(10):2222–2253.

[Moe et al., 2002] Moe, H., Ommundsen, A., and Gjevik, B. (2002). A high resolution tidal model for the area around the lofoten islands, northern norway. Continental Shelf Research, 22(3):485–504.

[Munk and Cartwright, 1966] Munk, W. H. and Cartwright, D. E. (1966). Tidal spectroscopy and prediction. Philosophical Transactions of the Royal Society of London. Series A, Mathematical and Physical Sciences, 259(1105):533–581.

[Naimie, 1996] Naimie, C. E. (1996). Georges bank residual circulation during weak and strong stratification periods: prognostic numerical model results. Journal of Geophysical Research: Oceans (1978–2012), 101(C3):6469–6486.

[Padman and Erofeeva, 2004] Padman, L. and Erofeeva, S. (2004). A barotropic inverse tidal model for the arctic ocean. Geophysical Research Letters, 31(2).

[Parker, 2007] Parker, B. (2007). Tidal analysis and prediction, noaa special publication nos co-ops3. silver spring, maryland. In Library of Congress Control, number 2007925298.

[Pawlowicz et al., 2002] Pawlowicz, R., Beardsley, B., and Lentz, S. (2002). Classical tidal harmonic analysis including error estimates in matlab using t_tide. Computers & Geosciences, 28(8):929–937.

[Polagye, 2013] Polagye, B. (2013). Implications of tidal phasing for power generation at a tidal energy site.

[Pugh, 1987] Pugh, D. T. (1987). Tides, Surges and Mean Eea-Level. John Wiley, Chichester, UK.

[Shchepetkin and McWilliams, 2005] Shchepetkin, A. F. and McWilliams, J. C. (2005). The regional oceanic modeling system (roms): a split-explicit, free-surface, topography-following-coordinate oceanic model. Ocean Modelling, 9(4):347–404.

[Theodoridis and Koutroumbas, 2008] Theodoridis, S. and Koutroumbas, K. (2008). Pattern Recognition. Elsevier Science.

[Tu et al., 2013] Tu, J., Yeoh, G. H., and Liu, C. (2013). Computational fluid dynamics: a practical approach. Butterworth-Heinemann.